7-2014

Characterization of Sinusoidal Vibration Induced Fluid Motion in Spherical Elastomeric Diaphragm Tanks

Cody Ambrose Harris

Characterization of Sinusoidal Vibration Induced Fluid Motion in Spherical Elastomeric Diaphragm Tanks

by

Cody Ambrose Harris

Bachelor of Science
Aerospace Engineering and Mathematical Science
Florida Institute of Technology
2013

A thesis
submitted to Florida Institute of Technology
in partial fulfillment of requirements
for the degree of

Master of Science
in
Aerospace Engineering

Melbourne, Florida
July 2014

We, the undersigned committee, hereby recommend
that the attached document by accepted as fulfilling in
part the requirements of the degree of
Master of Science in Aerospace Engineering

Characterization of Sinusoidal Vibration Induced Fluid Motion in Spherical Elastomeric Diaphragm Tanks

A thesis by Cody Ambrose Harris

_____

Daniel R. Kirk, Ph.D., Principal Advisor
Professor and Associate Department Head
Mechanical and Aerospace Engineering

_____

Hector M. Gutierrez, Ph.D.
Professor
Mechanical and Aerospace Engineering

_____

Lisa M. Perdigao, Ph.D.
Associate Professor
School of Arts and Communication, College of Psychology and Liberal Arts

_____

Hamid Hefazi, Ph.D.
Professor and Department Head
Mechanical and Aerospace Engineering

Abstract

Characterization of Sinusoidal Vibration Induced Fluid Motion in Spherical Elastomeric Diaphragm Tanks

by

Cody Ambrose Harris

Principal Advisor: Daniel R. Kirk, Ph.D.

Elastomeric diaphragm tanks are commonly used in spacecraft applications to incite positive expulsion of hydrazine monopropellant. The diaphragm exhibits low flexural rigidity, causing it to easily fold under its own weight at low fill levels. If the tank is sinusoidally oscillated under standard gravity, such as during ground transportation or launch pad winding, these folds will result in rubbing, eventually wearing down the thin material to the point of failure. The ability to accurately predict the presence of folds, rubs, and center of gravity shifts for a given tank design and frequency excitation is thus of critical importance to mission reliability, safety, and success. It is the objective of this thesis to determine the controlling aspects and parameters of the tank assembly which contribute to deformations and their functional relationship to the deformations, to validate this model, and to create a design evaluation method to ensure that the risk of diaphragm rubbing is mitigated. The current work proposes and implements an analytic technique to determine the governing parameters of the fluid-tank assembly as well as a computational scheme based on the inextensibility of the diaphragm and dominant parameters of the fluid phase to provide a highly efficient simulation of the fluid-structure interaction for the purposes of iterative design. Additionally, the current work develops an experimental framework for the validation of computational models and future tank designs, allowing for the complete characterization of the fluid distribution via analytic, computational, and experimental means. The computational model shows strong correlation with experimental data and is limited in generality only by the required spherical shape of the tank. This work can be expanded to allow other tank and diaphragm geometries to encompass all elastomeric diaphragm tank designs by developing abstract structured meshing techniques. This will serve to reduce development costs and increase confidence in mission success for al diaphragm tank-based spacecraft.

Table of Contents

List of Figures

List of Tables

List of Abbreviations

3D	Three-Dimensional
AFML	Air Force Materials Laboratory
ASAP	Aerospace Systems And Propulsion
ATK	Alliant Techsystems, Inc.
CAD	Computer Aided Design
CFD	Computational Fluid Dynamics
CG	Center of Gravity
CMM	Coordinate Measuring Machine
DMM	Dynamic Mesh Modeling
DOF	Degrees Of Freedom
EDT	Elastomeric Diaphragm Tank
EPDM	Ethylene Propylene Diene Modified
ESA	European Space Agency
FEA	Finite Element Analysis
FF	Fill Fraction
FIT	Florida Institute of Technology
FPS	Frames Per Second
FSI	Fluid Structure Interaction
IEEE	Institute of Electrical and Electronics Engineers
IMU	Inertial Measurement Unit
ISS	International Space Station
LCD	Liquid Crystal Display
NASA	National Aeronautics and Space Administration
ODE	Ordinary Differential Equation

PCIe	Peripheral Component Interface - express
PDE	Partial Differential Equation
PMD	Propellant Management Device
SPHERES	Synchronized Position Hold Engage Reorient Experimental Satellites
USB	Universal Serial Bus
VERTIGO	Visual Estimation and Relative Tracking for Inspection of Generic Objects
VOF	Volume Of Fluid

List of Symbols

A	amplitude [m]
a	acceleration [m/s^2]
Bo	Bond Number
c	wave speed [m/s]
E	modulus of elasticity of diaphragm [Pa]
F	force [N]
f	frequency [Hz]
Fr	Froude Number
g	acceleration due to gravity [m/s^2]
h	height [m]
i, j	mesh coordinates
k	spring stiffness [N/m]
L	undeformed length [m]
m	mass [kg]
p	pressure [Pa]
q	distributed load [Pa]
R	radius [m]
r	radial coordinate [m]
T	tension [N]
t	time [s]
u	vertical displacement [m]
$\vec{v}$	velocity [m/s]
V	volume [m^3]
x, y, z	Cartesian coordinates [m]

We	Weber Number
α, β	angle of inclination [rad]
δ	deformation [m]
θ	angular coordinate [rad]
κ	flexural rigidity [J]
ν	Poisson ratio of diaphragm
ρ	density [kg/m^3]
σ	surface tension [N/m]
τ	thickness of diaphragm [m]

Subscripts

b	base of tank *or* bending
d	diaphragm (or solid) phase
$diff$	difference between experimental and computational
eq	equivalent
p	propellant (or fluid) phase
0	reference condition

Superscripts

$*$	non-dimensionalized
0	shifted coordinate system

Acknowledgements

I wish to thank Drs. Dan Kirk, Hector Gutierrez, and Lisa Perdigao for their support in my academic endeavors, career aspirations, research interests, and the authoring of this thesis. Their support has made my graduate studies possible, and I trust their teachings, both curricular and extracurricular, will carry me for many years to come.

I also wish to thank my friends and family members for moral support throughout this process; the stresses of research are eased by the support of personal relations.

Finally, I wish to thank ATK Space Systems, Inc., for creating this research opportunity, allowing me to explore and expand my engineering skill set while providing useful results for the aerospace industry, and their financial support of this and related research endeavors conducted at the Florida Institute of Technology.

Chapter 1
Introduction

Propellant management systems in modern space vehicles counteract the effect of fluid slosh on vehicle trajectory by incorporating mechanisms to dampen slosh-induced vibrations [1]. One such mechanism employed by ATK Space Systems, Inc. in liquid hydrazine tanks for a variety of space vehicles utilizes a diaphragm made of Propylene Ethylene Diene Modified (EPDM) polymer, a hyperelastic rubber [2]. The diaphragm is secured within a spherical tank as shown in Figure 1 and contains the fluid within one hemisphere of the tank. The other side of the diaphragm is pressurized with a compressed gas to force fluid from the exhaust port at a controllable rate [3]. Non-spherical heads can also be used to lower the Center of Gravity (CG) of the tank [4].

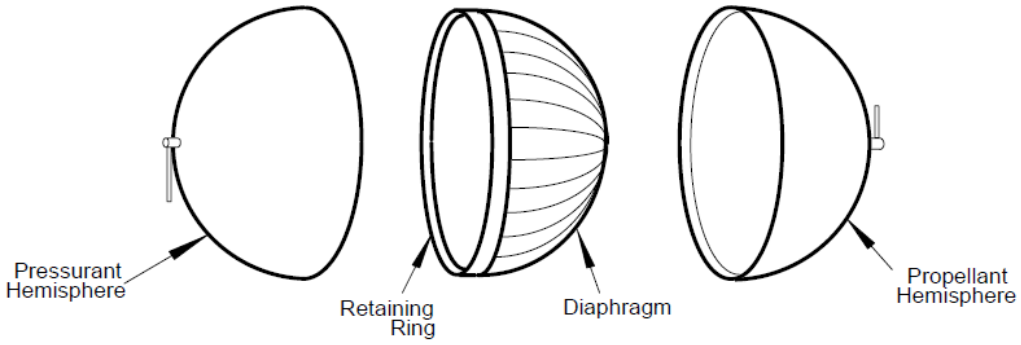

Figure 1 - Explosion View of Typical ATK Diaphragm Tank Assembly [3]

This rubber diaphragm is a flight-critical component since, should failure occur, slosh could displace fluid away from the exhaust port causing power interruption, or even cause fuel to enter the pressurant gas inlet and cause complete cessation of

thrust. The relatively thin membrane is most susceptible to failure as a result of material wear caused by the rubbing of the diaphragm against itself or the tank shell when folding occurs. It is thus critically important to reduce or eliminate the risk of rubbing caused by fluid slosh during vibrations which may be encountered by the tank during ground transportation, or as a result of wind while at the launch pad. However, with computational power only recently becoming sufficient to model the complexities of interactions between fluids and structures in response to slosh, almost no research exists on the predictive modeling of slosh in these diaphragm-based tank designs.

1.1 Motivation

ATK Space Systems, Inc. has produced scaled versions of the diaphragm-controlled spherical tank design for numerous space vehicles with tank diameters of up to forty inches. Some tanks also include a cylindrical section between the hemispheres, forming a "pill"-shaped tank with length-to-diameter ratios approaching 2:1 [5]. With such a wide variety of tanks to construct, it is critical to share components among the designs wherever practical to reduce manufacturing costs. As a result, ATK has utilized a constant diaphragm thickness which does not scale with the size of the tank. However, with rising concern for the weight of structures in the vehicle, it is desirable to reduce the weight of the diaphragm. For a current mid-size tank, the weight of the diaphragm is approximately 4.50 lbf, significantly more than other slosh control devices. However, if a minimal thickness diaphragm was used appropriate to the scale of the tank, this weight could be substantially reduced [3].

The minimal diaphragm thickness is certainly a function of the tank size. With the constant 0.06 inch thickness currently used for the material, experiments have

shown that deformations in the diaphragm are nearly unobservable in a sixteen inch diameter tank but are only marginally stable in a forty inch diameter tank. Neither situation is desirable – the over-damped system will be substantially heavier than it needs to be while the under-damped system is susceptible to folding, rubbing, and ultimately system failure.

To determine the ideal material thickness for an appropriately damped diaphragm, it is necessary to determine an analytic parameter which dictates whether folding and rubbing occur. By placing appropriate bounds on such a parameter, the thickness of the diaphragm will be constrained to a range which allows deformation but damps oscillations before rubbing occurs. A sequence of similar-sized tanks for which the allowable thickness range contains an overlap can be constructed from a single diaphragm stock of a thickness within the overlap region to reduce manufacturing costs, but dissimilar tanks must be constructed using different material stock. Thus the creation of such a rule-of-thumb boundary condition will keep low manufacturing costs, reduce tank weight and launch costs, and improve the safety and reliability of the flight-critical diaphragm component. ATK has thus sought the assistance of the Florida Institute of Technology (FIT), which has an eight-year heritage of modeling fluid slosh in other tank designs, to identify those design parameters and their corresponding limits that will eliminate concern for rubbing-induced material wear leading to diaphragm failure. The current work will focus on predictive modeling of the phenomenon so that continued research at ATK and FIT can numerically iterate design concepts intended to solve this problem.

1.2 Objective

For propellant management systems manufacturers and propulsion system development engineers, a method for determination of whether a diaphragm-controlled fluid containment system is stable under an applied vibration is of critical importance. Such a vibration, which is known to be incited during ground transportation and during countdown on the launch pad due to wind effects, could result in sufficient deformation of a hyperelastic diaphragm resulting in material failure. It is the objective of this thesis to determine the controlling aspects and parameters of the tank assembly which contribute to deformations and their functional relationship to the deformations, to validate this model, and to create a design evaluation method to ensure that the risk of diaphragm rubbing is mitigated. This is accomplished using an analytic approach to solve the governing equations modeling the diaphragm deformation to identify the non-dimensional controlling parameters, and a computational model. Finally, the steady state solutions will be verified experimentally utilizing an imaging system to capture the three-dimensional diaphragm shape at various fill levels for comparison to and validation of computational results. An overall summary of the tasks required to complete each of these objectives is outlined below.

1. Analytically identify the parameter or parameters, composed of physically-measurable attributes of the fluid-tank assembly, which fully dictate the response deformation of the hyperelastic diaphragm to a given oscillatory vibration.
    a. Determine the set of governing equations from the physical description of the situation that describe the behavior of the solid structure and the fluid contained within it.

b. Using appropriate boundary conditions and assumptions where required to make the governing equation solvable, obtain an explicit formulation for the geometric shape of the deformed diaphragm.
c. Non-dimensionalize the deformation equation and collect terms associated with the physical tank setup to form non-dimensional parameters.

2. Create a computational model of the diaphragm motion for both steady-state and transient sinusoidal oscillations which minimizes the loss of generality using input parameters representative of realistic propellant tanks using a coupled fluid and structure solving technique to determine the deformation response.
3. Design an experimental platform and associated procedure that allows for the variation of the selected parameters.
    a. Construct an Elastomeric Diaphragm Tank (EDT) such that the selected parameters can be independently varied to mimic the behavior of the widest possible array of realistic tank setups.
    b. Implement a vision-based or tactile instrumentation system which can identify the geometry of the diaphragm in its deformed state and export in a format appropriate for comparison to analytic and computational results.

1.3 Approach

To characterize the physical shape of the diaphragm, a static condition is first evaluated by considering a free-body view of a differential area of the diaphragm. Since hydrostatic forces are easily expressible analytically, a governing differential equation will be produced in closed form. With the known boundary condition at

the circumference of the tank, the problem becomes well-posed and can be solved uniquely. Once the final solution is determined, it is non-dimensionalized and the governing parameters are identified. A perturbation analysis is then conducted using dimensional analysis to determine the additional non-dimensional parameters which govern slosh motion.

The parameters which result from the static and transient analysis are consistent with assumptions and predictions made during previous studies at the Florida Institute of Technology (FIT), but it is desirable to validate these parameters with a numerical experiment. This is conducted using a fully coupled Fluid-Structure Interaction (FSI) simulation. Each of the variables which contribute to the parameters will be varied while holding the non-dimensional parameters constant to ensure the shape of the deformed diaphragm does not change.

The experimental platform will be constructed using a modified version of a mid-size EDT. The solid outer wall is made of clear plastic to facilitate optical instrumentation. A series of vision sensors are mounted to the tank assembly and create a full three-dimensional model of the diaphragm shape based on the images captured. The model can be used to validate analytic and computational deformation models.

1.4 Thesis Overview

The body of this thesis is organized in the sequence of the aforementioned objectives. The next chapter will highlight other research activities that have been conducted or are presently active in the analysis and development of EDTs and simulations of fully-coupled fluid-vehicle interaction. Chapter 3 will focus on the analytic approach in which the physical oscillation problem is reduced to a set of governing differential equations and boundary conditions, and an attempt is made

to solve this system with as little loss of generality as possible. Chapter 4 develops a computational scheme for the analysis of the system, coupling CFD and inextensible cloth modeling methods to analyze their joint motion. Chapter 5 discusses the design of the experimental apparatus and the associated instrumentation system for evaluating the influence of selected parameters on diaphragm deformations, and subsequent comparison to analytic and computational results. Finally, Chapter 6 will finalize these conclusions and comment on their applicability to future tank development.

Chapter 2
Background

ATK has conducted significant internal research and development throughout its history of developing EDTs, which have included development of special materials for the diaphragm, the addition of ridges to reduce adhesion and improve expulsive efficiency, and trade studies for the external tank shell shape. Slosh studies have been conducted on these tanks as well, with the predominant intention of ensuring the effectiveness of the diaphragm, not its endurance to rubbing. Other materials research has centered on the stress-strain relationship of circular clamped diaphragms, some analytic and some empirical. For computational analysis, a critical consideration is the coupling of fluid simulation and structures simulation. This coupling is not novel, but is difficult to apply to hyperelastic materials. Some research in complex geometry balloons has successfully demonstrated that this can be accomplished [6].

2.1 History and Development of EDTs

In principle, the goal of the propellant management device is to create a positive expulsion of propellant from the tank. This is naturally accomplished by creating a pressure gradient across the propellant such that positive expulsion is a favorable flow direction. Since the pressure at the outlet of the tank is a property of the downstream components, and thus inalterable, this is accomplished by increasing the pressure on the other side of the fluid. Since the tank operates in a microgravity environment, it is necessary to contain the fluid around the outlet, as adhesion

would naturally locate the fluid around the exterior of the cavity, not necessarily near the outlet. This could result in temporary fuel interruptions or loss of pressure in the pressurant gas. This must be accomplished by an elastomeric membrane, as the volumes of the two regions of the tank will change as propellant is expelled.

The membrane can be adhered to the exterior shell around the inlet to form a gas-containing bladder, the outlet to form a propellant-containing bladder, or around the mid-section to form a diaphragm. The bladder approaches minimize the sealing area and are easier to integrate in a larger system. However, as the bladder expands or contracts to account for volume changes, the surface area also changes significantly, and thus the force exerted by the pressurant gas alters. This results in inconsistent expulsion velocity, which is avoided by use of the diaphragm approach. The diaphragm is also a simpler geometry, allowing for easier manufacturing and less severe folding [7].

2.1.1 Diaphragm Material

EDTs throughout the industry have undergone a number of design iterations with regard to the material used for the diaphragm. In the 1950s and 1960s, a variety of readily available polymers were utilized by individual manufacturers, predominantly Voit Rubber Corporation and the Jet Propulsion Laboratory, based almost entirely on their chemical compatibility with hydrazine monopropellant. Most elastomeric materials dissolve over time in this volatile environment, so manufacturers sought materials with the longest half-life and the least harmful contaminants to the propellant. In1971, the Air Force Materials Laboratory (AFML) was contracted to find a suitable material. The result of this study was a variant of EPDM polymer termed AF-E-332. ATK unilaterally adopted this material as that of choice for EDT manufacturing. It has numerous desirable properties, including high tensile breaking and tear strengths, low density, and hyperelasticity [2]. A summary of its properties are presented in Table 1.

Table 1 - Mechanical Properties of AF-E-332 [3]

Property	Value
Tensile Strength	>11.4 MPa
Elongation at Break	>260%
Tear Strength	>52.5 kN/m
Hardness IRHD	90±5^{o}
Compression Set	<22%
Density (nominal)	1.10 g/cc

AF-E-332 was the exclusive EPDM polymer in EDTs for several decades of their flight heritage. However, around the turn of the millennium, it was discovered that in tanks which use this material, the hydrazine contains leached silicon contaminants after only a few years. This is somewhat surprising, as silicon is not an elemental ingredient in EPDM polymer. It is presently believed that this contaminant originates from a filler used in the synthesis of the compound, which cannot be altered [8]. In order to meet design specifications for upcoming applications in satellites produced by the European Space Agency (ESA), ATK sought a material with mechanical properties identical to those of AF-E-332 but which does not leach silicon. This gave rise to the material used over the last decade in all EDTs, termed SIFA-35 [2]. Its material properties are summarized in Table 2.

Table 2 - Mechanical Properties of SIFA-35 [3]

Property	Value
Tensile Strength	>11.4 MPa
Elongation at Break	>240%
Tear Strength	>52.5 kN/m
Hardness IRHD	90±5°
Compression Set	<22%
Density (nominal)	1.12 g/cc

Although SIFA-35 does have a reduced elongation at break as compared to AF-E-332, it was determined that this would not critically alter the applicability of the material, and SIFA-35 has since obtained a respectable flight heritage of its own over the last decade.

2.1.2 Alternative Method for Propellant Management

While the use of a membrane material to encite positive expulsion of propellant is a natural step for the posed design problem, alternative methods exist. ATK also manufactures Propellant Management Device (PMD) tanks, which utilize a subassembly of vanes around the tank outlet and rely on surface tension of the fluid, manipulated by the vanes, to drive the fluid motion. Despite the decade-long head start given to EDTs, PMD tanks have surpassed their membrane-based brethren in manufactured quantity and continue to rise in popularity as a very viable alternative. A schematic representation of a PMD tank is shown in Figure 2 [9].

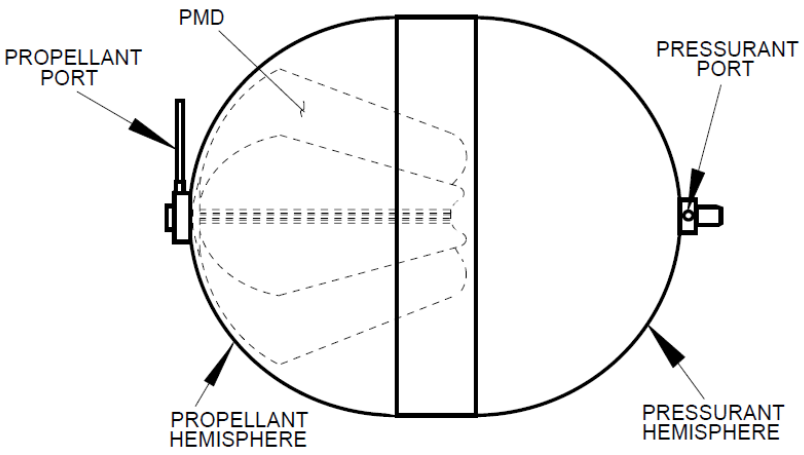

Figure 2 - Schematic Representation of PMD Tank [9]

It is difficult to ascertain the relative reliability of PMD tanks and EDTs. It is generally agreed that the lack of moving parts in the passive PMD tank cause it to be significantly more reliable, but each PMD is tailor-made for a specific mission application, while EDTs are relatively standardized in design. Complicating the matter, PMDs cannot be ground-tested due to their reliance on microgravity, which limits the sample size of tanks that can be analyzed for reliability.

PMD tanks have an unquestionable advantage in scaling ability. Tanks of virtually any size can be produced, although modifications to the PMD based on the shell geometry may be necessary. EDTs, however, are limited to diameters on the order of forty inches, with a maximum length-to-diameter ratio of 2:1, in order to maintain stability of the diaphragm.

If the folding stability problem of large diaphragms were solved, EDTs offer several advantages over equivalent PMD tanks. EDTs have expulsion efficiencies of 99.9%, while PMD tanks are estimated at 99.7%. Diaphragm tanks also offer an incomparable level of slosh control, retaining fluid in the appropriate hemisphere of the tank and ensuring gas-free expulsion, while PMD tanks can only offer comparable control with the introduction of dampers and baffles, which introduce

expulsion inefficiencies and added mass and complexity. Additionally, despite the recurring costs of EDTs exceeding that of PMD tanks due to the diaphragm mold, EDTs are well-developed and diversified, whereas PMD tanks are frequently newly developed for mission-specific applications. The additional research costs make EDTs a cost-effective design for low-quantity manufacturing, which is typically experienced in the spacecraft industry [3].

2.1.3 Slosh Experiments on EDTs

During the design process of new EDTs, ATK conducts vibration testing to determine how slosh will affect tank performance. The test is intended to ensure gas-free expulsion during operation, but can be adapted to observe folding and rubbing of the diaphragm by using a clear tank shell. The setup of the experiments performed by ATK is depicted in Figure 3.

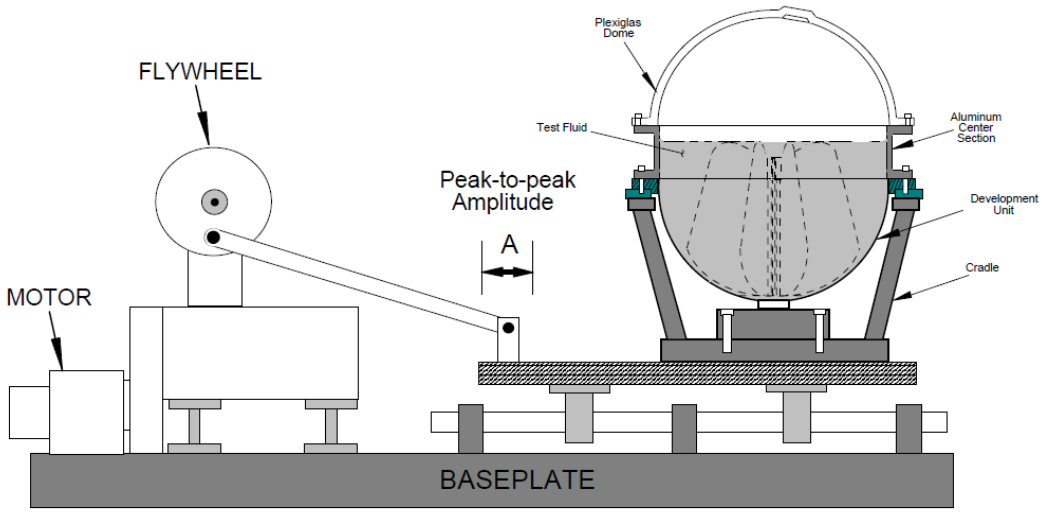

Figure 3 - Experimental Setup for Slosh Evaluation of New ATK Tanks [7

Although slosh testing has been extensive with rigid tanks, little information is available on the influence of slosh on hyperelastic membranes. Testing conducted

on EDTs by ATK has revealed two key observations. First, the ability of the diaphragm to dampen sloshing is the result almost exclusively of the viscoelasticity of the diaphragm and not the viscosity of the fluid. Second, the shape of the deformed diaphragm in a given tank is a function of the volume of fluid, generally expressed as a Fill Fraction (FF), and is independent of the fluid density. In essence, the slosh behavior is independent of any intensive property of the propellant, and is a function instead of the tank itself, the vibration applied, and the FF. This order-of magnitude analysis will be critical to the analytic characterization of the interaction of the propellant and diaphragm under an applied vibration [3].

2.2 Deformation of Elastomeric Membranes

While a closed-form analytic solution does not presently exist for a hyperelastic circular membrane under a distributed hydrostatic loading, analytic and empirical models for similar loadings exist and can be used as a guide for characterization. Most of these models are designed for non-hyperelastic materials, in which the assumption of minimal deformation is made. This allows certain applications of small-angle approximations in the free body analysis of a differential membrane element as well as the approximation of a distributed hydrostatic loading by a uniform distribution. Thus, the small deformation approximation severely limits the region of validity for these models. Literature also exists on the computational modeling of fluids and hyperelastic structures with complex geometries, which are discussed in Section 2.2.3.

2.2.1 Analytic Models

Analytic plate deflection theory is based on the Kirchhoff-Love relation, which utilizes the flexural rigidity of the material as a key material property [10]. Flexural rigidity is given by Eq. (2.1).

$$\kappa = \frac{E\tau^3}{12(1-v^2)} \tag{2.1}$$

In practice, the flexural rigidity of the diaphragm is extremely low. This results in unstable behavior of equations based on the flexural rigidity, which begin to exhibit non-linear behavior. Hence, existing analytic models will not suffice for analysis of EDTs, but may lend themselves to forms for empirical models of larger deflections.

The first analysis is conducted for small deflections up to one-fifth the diaphragm thickness. A uniform pressure is applied over the surface, which is rigidly clamped at its perimeter. The resulting equation is given by [11] in Eq. (2.2)

$$u(r) = \frac{qR^4}{64\kappa}\left[1 - \left(\frac{r}{R}\right)^2\right]^2 \tag{2.2}$$

As the assumption of small deflections is relaxed to allow deformations up to one-half the diaphragm thickness, the leading coefficient becomes complex, and it is useful to give it the symbol f [10].

$$u(r) = f\left[1 - \left(\frac{r}{R}\right)^2\right]^2 \tag{2.3}$$

The coefficient is given by

$$f = \left(-\frac{\beta}{2} + \gamma\right)^{\frac{1}{3}} + \left(-\frac{\beta}{2} - \gamma\right)^{\frac{1}{3}} \tag{2.4}$$

$$\gamma = \sqrt{\frac{\alpha^3}{27} + \frac{\beta^2}{4}} \tag{2.5}$$

$$\alpha = 14\frac{4\tau^2 + 3R^2\varepsilon_i(1+v)}{(1+v)(23-9v)} \tag{2.6}$$

$$\beta = \frac{-7qR^4t^2}{8\kappa(1+v)(23-9v)} \tag{2.7}$$

Clearly the coefficient will become increasing more complicated as the assumption continues to relax. As actual deformations experienced in EDTs are on the order of 300 times the diaphragm thickness, it is evident that elastic theory analytic techniques will not be suitable for characterizing EDTs.

2.2.2 Empirical Models

Analytic models, while they can account for a certain degree of large deflections, cannot account for diaphragm stress, which represents the stress along the middle of the diaphragm and becomes relevant only when the deflection exceeds one-half of its own thickness. Accounting for both diaphragm and bearing stress, but still restricting to a uniform pressure, the relation is given by [12] in Eq. (2.8)

$$u = \tau\left(\frac{pR^4}{3.44E\tau^4}\right)^{\frac{1}{3}}\left(1 - 0.9\frac{r^2}{R^2} - 0.1\frac{r^5}{R^5}\right) \tag{2.8}$$

This has been derived empirically through experiments utilizing a fifth-order polynomial regression to calculate the maximum deflection and the radial deflection profile. It is useful for the analysis of diaphragm deformations under uniform pressure loads such as aluminum diaphragms in a shock tube, but are still not applicable to the much larger deflections in an elastomeric diaphragm.

2.2.3 Computational Model

Computational work in propellant slosh for spacecraft applications is extensive, utilizing modern computing power to solve complex fluid motion; however, these models have largely been employed on uncontained fluid tanks. No published research yet characterizes the motion experienced within EDTs. The use of a Volume Of Fluid (VOF) approach to model the interfacial free surface of two fluid phases has allowed numerous parametric slosh studies to be conducted numerically, as well as providing predictions to be benchmarked by experimental data. However, in the case of EDTs, the boundary conditions to the fluid solver will be highly dynamic as a result of diaphragm deformations, which must be modeled using a separate computational mechanics simulation. SIFA-35 exhibits a highly non-linear stress-strain relationship and a very low flexural rigidity. These factors combine to create instabilities in most Finite Element Analysis (FEA) algorithms, as the large deformations in such a material are highly non-linear. However, some success has been achieved by noting that the low flexural rigidity causes the diaphragm to resist stretching and shrinking, opting instead for bending to conform to the fluid shape. Past work at Embry-Riddle Aeronautical University has theorized that this allows the elastic non-linearity of the diaphragm material to be neglected, simplifying the problem tremendously and reducing the tendency towards divergence [14]. Ongoing work at Florida Institute of Technology has suggested that the diaphragm behaves as entirely inextensible, and its elasticity can be eliminated altogether [13]. Alternate algorithms for inextensible materials will thus be the focus of the current work, and are detailed in Chapter 4.

The traditional methods for structure modeling using FEA and its coupling with CFD are not appropriate for this analysis, as the stability of FEA is directly dependent on the flexural rigidity. The large deformations exhibited tend to diverge all FEA schemes. When large bending occurs in a nearly inextensible material, the bending can only be modeled by a gradient of strain across the thickness of the

membrane. To smoothly model this, the spatial resolution must be large enough that several nodes exist within the thickness of the diaphragm. This results in millions of total nodes across the entire surface, requiring large computational time. Exacerbating the problem, stability criteria require that the temporal resolution increase with the spatial resolution, reducing the maximum timestep to mere nanoseconds. Limited success was achieved in simple test cases, as shown in Figure 4, but the convergence time, on the order of days or even weeks, makes the scheme impractical for steady-state studies and inappropriate for transient studies [13],[14].

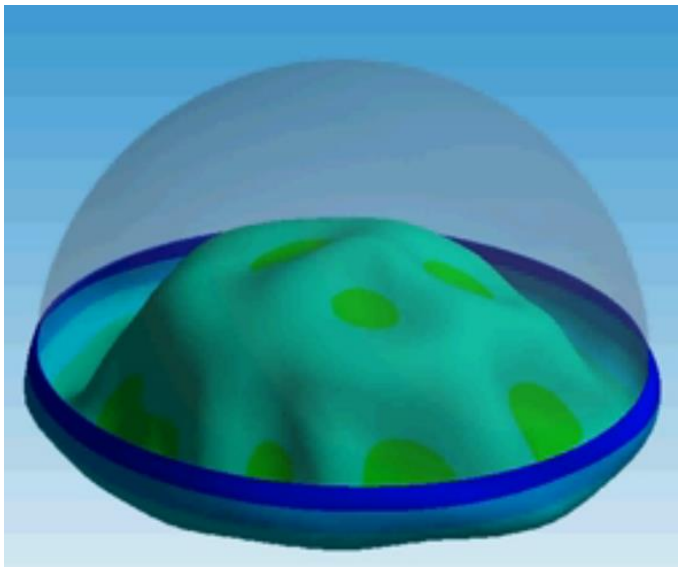

Figure 4 - Successful FEA-CFD Model of Steady-State Elastomeric Diaphragm Tank [13]

2.3 Related Research at Florida Institute of Technology

Florida Institute of Technology (FIT) has been actively studying fluid slosh dynamics and its applications in propulsion system design in the Aerospace Systems And Propulsion (ASAP) Laboratory since 2006. Early studies were conducted in response to a finding by a joint task force of Boeing, NASA, and

Analex Corporation that revealed a potential design fault in the Boeing Delta IV Heavy due to an erroneous slosh simulation [15]. A variety of experimental and numerical frameworks were developed as part of these studies, including increasing degrees of freedom and a higher fidelity of testing environment. Capitalizing on the wealth of knowledge and testing equipment amassed by FIT, ATK has consulted the ASAP Laboratory to further understand the slosh behavior within EDTs and how this may be contributing to undue wear and tear of diaphragms before launch, ultimately targeting a solution to this phenomenon.

2.3.1 Preliminary Slosh Studies

Initial slosh studies at FIT were concerned with the development of numerical and experimental frameworks that could be used for future slosh studies. Two types of problems were examined:

1. Forced motion in which the position, velocity, and acceleration time histories of the tank are predetermined, and an idealized actuation system is utilized to force them to occur as defined, independent of forces or moments caused by fluid sloshing events.
2. Free motion in which only the forces applied to the tank from external sources are known, but the motion of the tank is allowed to vary as a result of internal forces and moments caused by fluid sloshing events.

The second mode of motion introduced the need for numerical simulations of fluid-vehicle interaction. A rigid-body kinematic simulation could simulate the motion of the tank in response to the pressure and body force distribution of the fluid. Similarly, the motion of the fluid in response to the moving tank could be computed using the VOF method. This method tracks bulk fluid motion by defining the free interface surface of a fixed volume of fluid within a stationary or moving mesh. It does not, however, allow for the calculation of fluid motion within that

volume unless combined with the Navier-Stokes equations. However, this is not necessary for the purpose of slosh studies [16].

With a numerical scheme for the rigid-body analysis and fluid analysis selected, they needed to be coupled. This was accomplished using a staggered iteration method known as Dynamic Mesh Modeling (DMM). In this scheme, as depicted in Figure 5, the VOF equations are solved first. The solution to an iteration of the VOF equations, discretized using finite differencing, are then used to compute the forces acting on the tank due to fluid pressure. These are used as inputs to the rigid body kinematic equations, which are used to compute the resultant tank position. This, in turn, feeds back as the moving mesh of the VOF discretization. The process iterates until convergence is achieved.

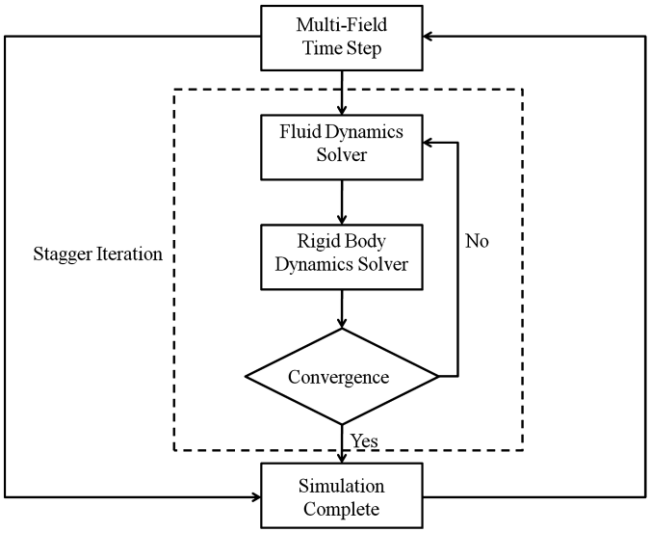

Figure 5 - Block Diagram of Dynamic Mesh Modeling Algorithm [16]

This numerical scheme must be benchmarked against experimental data. Experiments performed at the ASAP Laboratory included forced and free motion along one translational axis and, for free motion, one rotational axis. The experimental apparatus is depicted in Figure 6 [17],

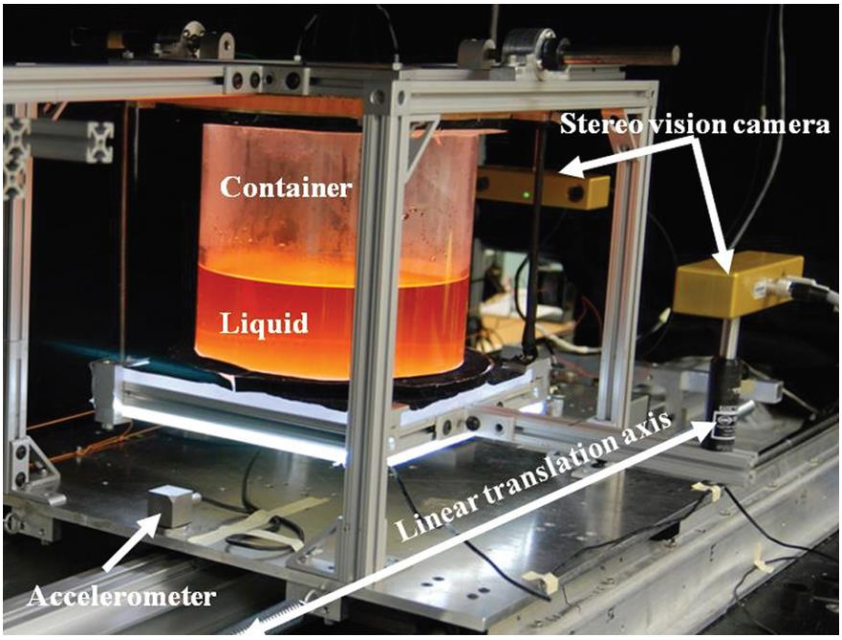

Figure 6 - Experimental Setup of 1D Motion Table [17]

The computer controlled motion table creates the desired kinematic profile. The accelerations are recorded by on-board Inertial Measurement Units (IMUs) and used as input to the numerical simulation. The tank is imaged using two orthogonally mounted stereo vision cameras. Images and numerical results at fixed times within the experiment are then compared to determine the agreement of the numerical model with experimental data. The agreement is strong, on the order of $\pm 3\%$.

With the experimental and numerical platforms created, studies into potential methods for reducing slosh were investigated. In particular, a parametric study of tank baffles was conducted utilizing the DMM method. As shown in Figure 7, the introduction of a baffle causes sloshing fluid to be redirected back into the bulk fluid, reducing the effect on CG shifting and the possibility of fluid entering the forward compartment of the tank, where venting is usually contained. The study

investigated the sizing, placement, and quantity of baffles to use for the most effective slosh control [18].

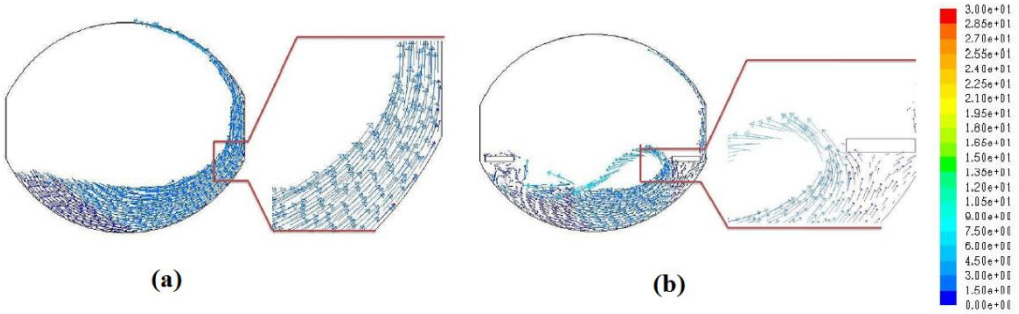

Figure 7 - Comparison of (a) Smooth and (b) Baffled Tank Velocity Field During Slosh Event [18]

As slosh studies in the ASAP Laboratory evolved, additional modes of motion needed to be studied using the numerical tools, but no experimental benchmarks existed. The motion table, which supported two Degrees Of Freedom (DOF), was thus modified to support four DOF; a nutation mode and a second rotation mode were added. The new platform, depicted in Figure 8, provided the necessary benchmark to utilize the DMM scheme for more advanced studies.

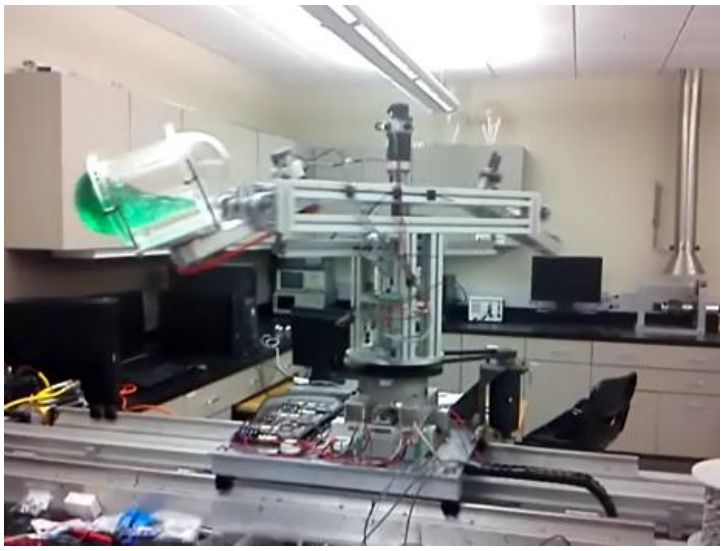

Figure 8 - 4 DOF Nutation Slosh Testing Apparatus

2.3.2 Slosh Experimentation in Microgravity

Given the Analex study of the Boeing Delta IV Heavy launch vehicle which motivated the initial slosh research at FIT it became necessary to apply the computational models to a microgravity environment, as this is the environment in which this fuel tank operates and is subjected to slosh-inducing maneuvers. As with other computational advancements, it is necessary to benchmark the model using experimental data obtained in a microgravity environment. To accomplish this, an experiment was performed aboard aircraft utilizing a parabolic flight trajectory to induce brief periods of microgravity. In order to keep size at a minimum, a motion platform could not be constructed. Instead, the initial motion was induced by the motion of the airplane itself as it entered the microgravity phase. These accelerations were tracked using IMUs, while fluid distribution was recorded using stereoscopic camera imaging. Agreement with the computational model was achieved, with a discrepancy of $\pm 8\%$ [19].

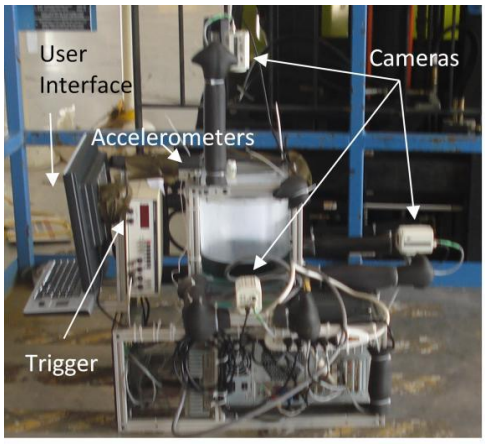

Figure 9 - Slosh Experiment for Reduced Gravity Aircraft Testing [19]

The microgravity emulation obtained by parabolic flight trajectories is severely limited in stability and duration. Fluctuations on the order of $\pm 0.2g$ can occur

throughout the period, which is limited to only 22 seconds. In order to truly benchmark computational models and allow full determination of fluid-structure interaction, a free-floating platform must be utilized in a sustained microgravity environment. Some initial studies were conducted using sounding rockets [20], but this is still limited in duration. The ideal testing laboratory for such experiments is the International Space Station (ISS). The SPHERES-Slosh project, depicted in Figure 10, was thus developed to enable such testing [21].

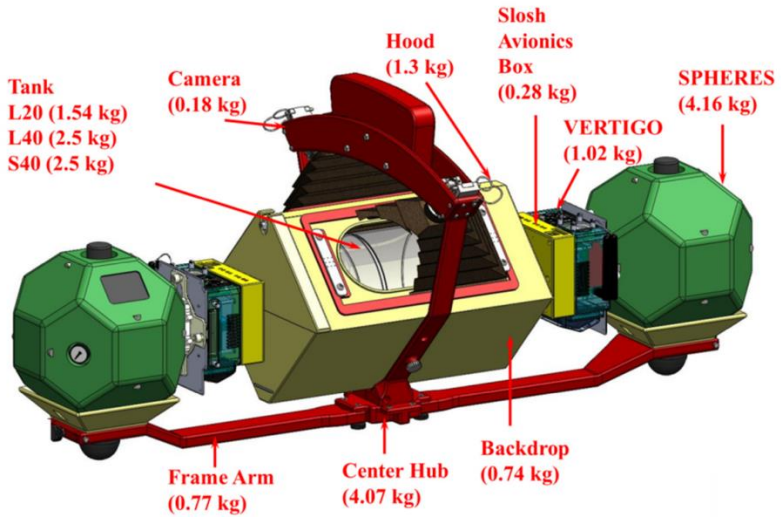

Figure 10 - SPHERES Slosh Experiment for International Space Station [22]

To minimize launch weight, a critical design constraint was to utilize existing hardware already available on the ISS. For this reason, the platform utilizes the Synchronized Position Hold Engage Reorient Experimental Satellites (SPHERES) to provide the thrusting and navigation, and the Visual Estimation and Relative Tracking for Inspection of Generic Objects (VERTIGO) data acquisition computers to store IMU data and stereoscopic camera images. The experiment is still ongoing, and data is not yet available to ascertain the agreement with computational models [23].

2.3.3 Slosh Evaluation of EDTs

Research at FIT into the characterization of slosh dynamics in EDTs is focused on ground transportation rather than in-flight maneuvers, and thus ground testing is appropriate to benchmark computational models. The current work takes a mathematical approach, both analytically and computationally, to the EDT slosh problem, but initial research was predominantly experimental to understand diaphragm behavior and relevant parameters. A forty inch EDT was installed in a large truck, equipped with IMUs and stereoscopic imaging cameras. While not a strictly controlled experiment, this work allowed the initial characterization of the behavior, and provided useful data on the accelerations and frequencies excited in large trucks carrying EDTs. Results suggested that folding and rubbing could be reduced by rotating the tank to other orientations, but this is not always practical.

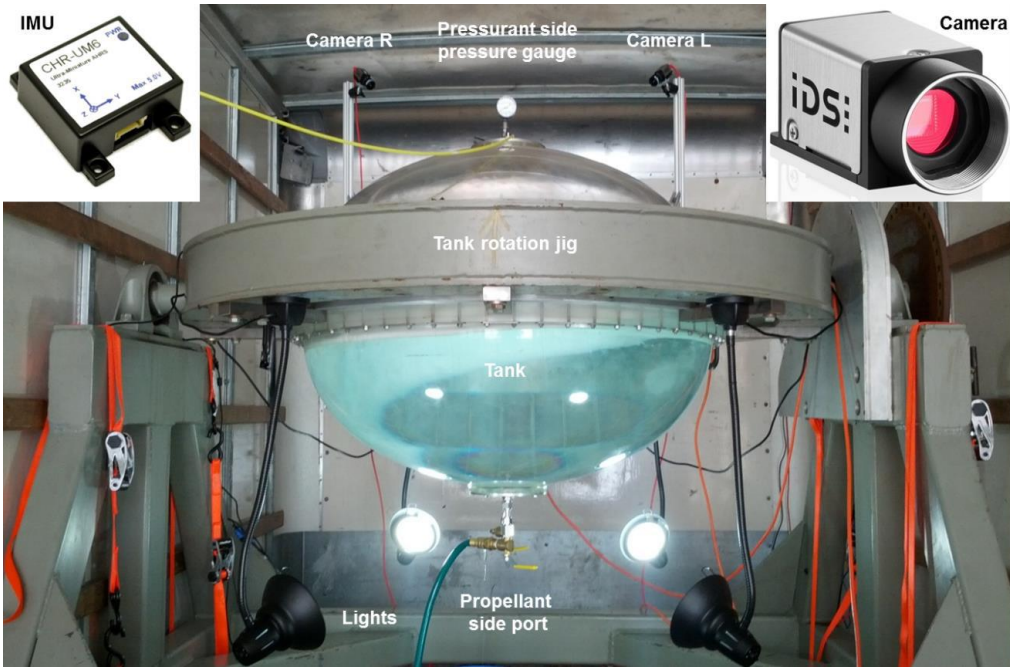

Figure 11 - 40-inch EDT in Ground Transportation Slosh Testing

2.4 Chapter Summary

As shown, research in slosh dynamics of non-constrained fluid tanks has clearly been extensive throughout the industry and at Florida Institute of Technology. Work performed by AFML has centered on the selection of the material for the diaphragm, providing strong mechanical properties to resist tearing while ensuring hydrazine chemical compatibility. The alternative method for reducing slosh and creating positive expulsion using capillary action have been investigated, based on systems of vanes and baffles. These methods have proven effective and have risen in popularity, but other disadvantages make the EDT still the tank of choice for a variety of spacecraft applications. With rising concerns for slosh control in propellant tanks, the slosh behavior of EDTs is of critical importance.

Models exist for diaphragm deformations in both an analytic and experimental model, but these models are limited to very small deformations that are not applicable to EDTs. Existing computational models are still under development, with attempts to capitalize on the inextensible behavior of the diaphragm currently allowing strides in improving computational efficiency. Once the structureal simulation is complete, integration with a flow solver can be accomplished using models already developed by FIT. These models have been used in non-diaphragm tanks to predict the behavior of a number of slosh tanks, and experiments have been conducted to benchmark these models. Increasing fidelity of the testing environment has demonstrated to the industry the accuracy of the model and its reliability for future use in propellant tank design. Similarly, the model will be benchmarked against experimental data from EDTs. To prepare for this, simple experimental studies are already being conducted with EDTs to gain familiarity with their slosh behavior.

Chapter 3
Analytic Solution

To fully describe the vibration-induced fluid motion in an EDT mathematically would require the conservation of mass and momentum to be applied to the propellant subject to the varying boundary condition caused by the moving diaphragm. This boundary condition, in turn, would be defined by the nonlinear version of Hooke's Law in three dimensions, which is itself a system of differential equations. The forcing function in Hooke's Law would be the pressure distribution caused by the fluid, which was determined from the conservation laws. This vicious cycle creates a fully-coupled set of Partial Differential Equations (PDEs) with complex boundary conditions and to date has not be solved analytically. However, seeking only to characterize the flow using analytic parameters, reasonable assumptions can be made. The key assumption which permits the system to be solved is that of zero flexural rigidity on a taut diaphragm. This implies that the distributed forces along the edges of a differential element of the diaphragm are everywhere tangent to the diaphragm- any deviation from this would result in the curving of the diaphragm. For larger tanks, where the thickness becomes relatively smaller, the flexural rigidity does decrease. However, a loss of generality for smaller tanks does result. Additionally, the assumption of a taut diaphragm restricts applicability to large FFs.

3.1 Governing Equations

Analysis of the fluid motion begins with the selection of a differential area of the diaphragm. As depicted in Figure 12, the differential area selected has dimensions of Δx and Δy.

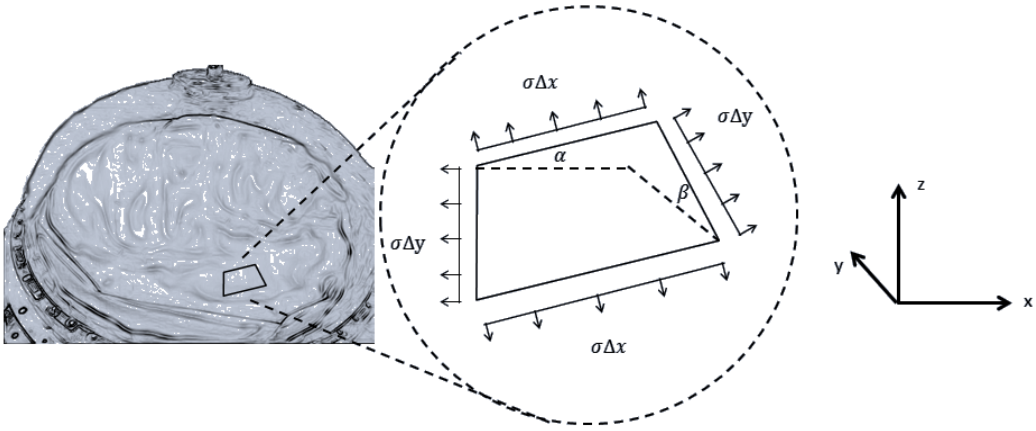

Figure 12 - Differential Area and Free Body Diagram

The tension of the diaphragm is taken to be σ in units of force per unit length. This tension, which occurs at the surface of the fluid, must also equal the fluid surface tension. The forces on the sides of the differential area are then $\sigma\Delta x$ and $\sigma\Delta y$ as shown. The differential area is taken to be a height of u from the neutral plane, inclined at an angle α from the x-axis, and an angle β from the y-axis. In the steady state evaluation, these angles are taken to be sufficiently small that $\sin\alpha \approx \tan\alpha$ and likewise for β.

Newton's second law in the Lagrangian reference frame is applied to the differential area about the z-axis. Thus

$$\Sigma F_z = \rho_d \tau \Delta x \Delta y \frac{\partial^2 u}{\partial t^2} \tag{3.1}$$

The net force in the z-direction is given by

$$(\Sigma F_z)_{edges} = -\sigma\Delta y \sin\alpha_{left} + \sigma\Delta y \sin\alpha_{right} - \sigma\Delta x \sin\beta_{front} + \sigma\Delta x \sin\beta_{rear} \tag{3.2}$$

The subscripts allow for slight variation in the angle of inclination over the differential area. Factoring out the common terms and substituting the small angle approximation,

$$(\Sigma F_z)_{edges} = \sigma\left[\Delta y\left(\tan\alpha_{right} - \tan\alpha_{left}\right) + \Delta x\left(\tan\beta_{rear} - \tan\beta_{front}\right)\right] \tag{3.3}$$

However, the tangent function is simply the slope, or derivative, of the diaphragm in the corresponding direction. Specifically, $\tan\alpha = \frac{\partial u}{\partial x}$ and $\tan\beta = \frac{\partial u}{\partial y}$. Thus,

$$(\Sigma F_z)_{edges} = \sigma\left[\Delta y\left(\frac{\partial u(x+\Delta x, y)}{\partial x} - \frac{\partial u(x,y)}{\partial x}\right) + \Delta x\left(\frac{\partial u(x, y+\Delta y)}{\partial y} - \frac{\partial u(x,y)}{\partial y}\right)\right] \tag{3.4}$$

Dividing by the area of the differential segment,

$$\frac{(\Sigma F_z)_{edges}}{\Delta x\Delta y} = \sigma\left[\frac{1}{\Delta x}\left(\frac{\partial u(x+\Delta x, y)}{\partial x} - \frac{\partial u(x,y)}{\partial x}\right) + \frac{1}{\Delta y}\left(\frac{\partial u(x, y+\Delta y)}{\partial y} - \frac{\partial u(x,y)}{\partial y}\right)\right] \tag{3.5}$$

Taking the limit as the size of the element approaches zero (i.e. $\Delta x, \Delta y \to 0$),

$$\frac{(\Sigma F_z)_{edges}}{\text{dxdy}} = \sigma\left(\frac{\partial^2 u}{\partial x^2} + \frac{\partial^2 u}{\partial y^2}\right) \tag{3.6}$$

In addition to the distributed forces on the edges of the differential element, a distributed force along the faces of the element is also possible, and would exist on the diaphragm due to hydrostatic pressure. The force is taken to have magnitude q in units of force per unit area. Thus the total force has a magnitude of $qdxdy$. The component in the z-direction is given by

$$(\Sigma F_z)_{faces} = qdxdy\cos\alpha\cos\beta \tag{3.7}$$

However, due to the small angle approximation, $\cos\alpha \approx \cos\beta \approx 1$. Thus,

$$\begin{aligned}\frac{\Sigma F_z}{dxdy} &= \frac{(\Sigma F_z)_{edges} + (\Sigma F_z)_{faces}}{dxdy} \\ &= \sigma\left(\frac{\partial^2 u}{\partial x^2} + \frac{\partial^2 u}{\partial y^2}\right) + q\end{aligned} \tag{3.8}$$

Substituting into Newton's second law,

$$\rho_d \tau \frac{\partial^2 u}{\partial t^2} = \sigma\left(\frac{\partial^2 u}{\partial x^2} + \frac{\partial^2 u}{\partial y^2}\right) + q \tag{3.9}$$

Or,

$$\frac{\partial^2 u}{\partial t^2} = \frac{\sigma}{\rho_d \tau}\left(\frac{\partial^2 u}{\partial x^2} + \frac{\partial^2 u}{\partial y^2}\right) + \frac{q}{\rho_d \tau} \tag{3.10}$$

Defining the wave speed $c = \sqrt{\sigma/\rho_d \tau}$,

$$\frac{\partial^2 u}{\partial t^2} = c^2 \left(\frac{\partial^2 u}{\partial x^2} + \frac{\partial^2 u}{\partial y^2} \right) + \frac{q}{\rho_d \tau} \tag{3.11}$$

Although the tank under study is spherical, the strictly axisymmetric nature of the diaphragm deformation under static conditions lends itself to a cylindrical formulation. Substituting $x = r\cos\theta$ and $y = r\sin\theta$,

$$\frac{\partial^2 u}{\partial t^2} = c^2 \left(\frac{\partial^2 u}{\partial r^2} + \frac{1}{r}\frac{\partial u}{\partial r} + \frac{1}{r^2}\frac{\partial^2 u}{\partial \theta^2} \right) + \frac{q}{\rho_d \tau} \tag{3.12}$$

Finally, due to the axisymmetric nature, derivatives taken with respect to θ are negligible. Additionally, the pressure distribution over the diaphragm will be solely a function of radial position. Thus the final governing partial differential equation for the diaphragm geometry is given by

$$\frac{\partial^2 u}{\partial t^2} = c^2 \left(\frac{\partial^2 u}{\partial r^2} + \frac{1}{r}\frac{\partial u}{\partial r} \right) + \frac{q(r)}{\rho_d \tau} \tag{3.13}$$

3.2 Steady-State Analysis

The pressure distribution for an incompressible fluid in a spherical tank will be given by

$$q(r) = p_0 - \rho_p g u \tag{3.14}$$

And therefore the final governing partial differential equation with a fluid-induced pressure gradient is given by

$$\frac{\partial^2 u}{\partial t^2} = c^2\left(\frac{\partial^2 u}{\partial r^2} + \frac{1}{r}\frac{\partial u}{\partial r}\right) - \frac{\rho_p g u}{\rho_d \tau} + \frac{p_0}{\rho_d \tau} \tag{3.15}$$

The last monomial of this expression is a constant, thus making the PDE nonhomogeneous. The general solution will thus take the form of the sum of the general solution of the associated homogeneous PDE and a particular solution to this PDE. The associated homogeneous PDE is given by

$$\frac{\partial^2 u}{\partial t^2} = c^2\left(\frac{\partial^2 u}{\partial r^2} + \frac{1}{r}\frac{\partial u}{\partial r}\right) - \frac{\rho_p g u}{\rho_d \tau} \tag{3.16}$$

Since only the steady-state condition is desired, the initial condition is not relevant, and assumed to be a relaxed diaphragm. It should be noted that this process eliminated any physical meaning associated with the time history of the function, and only the fully-converged, steady-state condition should be evaluated. Thus the auxiliary conditions are:

$$u(R_d, t) = u(r, 0) = 0 \tag{3.17}$$

Assuming a product solution of the form $u(r,t) = R(r)T(t)$, The PDE becomes the following system of Ordinary Differential Equations (ODEs):

$$RT'' = c^2\left(R''T + \frac{1}{r}R'T\right) - \frac{\rho_p g R T}{\rho_d \tau} \tag{3.18}$$

$$\frac{T''}{T} = c^2\frac{R''}{R} + c^2\frac{R'}{rR} - \frac{\rho_p g}{\rho_d \tau} = -\lambda \tag{3.19}$$

Where λ, the eigenvalue of the problem, is a constant independent of r and t. Thus there is now a separated system of ODEs

$$T'' + \lambda T = 0 \qquad r^2R'' + rR' + \frac{r^2}{c^2}\left(\lambda - \frac{\rho_p g}{\rho_d \tau}\right)R = 0 \tag{3.20}$$

We recognize the R-equation as Bessel's equation of order 0, which has the general solution

$$R(r) = c_1 J_0\left(\frac{r}{c}\sqrt{\lambda - \frac{\rho_p g}{\rho_d \tau}}\right) + c_2 Y_0\left(\frac{r}{c}\sqrt{\lambda - \frac{\rho_p g}{\rho_d \tau}}\right) \tag{3.21}$$

However, the Bessel function Y_0 approaches infinity for infinitesimal values of r, and therefore cannot contribute to a physically meaningful solution. Thus $c_2 = 0$. To satisfy the boundary condition, then,

$$J_0\left(\frac{R_d}{c}\sqrt{\lambda - \frac{\rho_p g}{\rho_d \tau}}\right) = 0 \tag{3.22}$$

Letting k_n represent the *n*th real zero of the Bessel function J_0, we find all possible eigenvalues to be of the form

$$\lambda_n = \left(\frac{ck_n}{R_d}\right)^2 + \frac{\rho_p g}{\rho_d \tau} \tag{3.23}$$

Therefore the eigenfunctions are of the form

$$R(r) = J_0\left(\frac{k_n r}{R_d}\right) \tag{3.24}$$

Substituting the eigenvalue, the T-equation becomes

$$T'' + \left[\left(\frac{ck_n}{R_d}\right)^2 + \frac{\rho_p g}{\rho_d \tau}\right] T = 0 \tag{3.25}$$

This ODE has the general solution

$$\begin{aligned} T(t) = c_3 \cos\left(t\sqrt{\left(\frac{ck_n}{R_d}\right)^2 + \frac{\rho_p g}{\rho_d \tau}}\right) \\ + c_4 \sin\left(t\sqrt{\left(\frac{ck_n}{R_d}\right)^2 + \frac{\rho_p g}{\rho_d \tau}}\right) \end{aligned} \tag{3.26}$$

This gives a final solution to the full equation including a particular solution $p(r,t)$ of

$$
\begin{aligned}
&u(r,t)\\
&= p(r,t)\\
&+ \sum_{n=1}^{\infty} J_0\left(\frac{k_n r}{R_d}\right)\left[c_3 \cos\left(t\sqrt{\left(\frac{ck_n}{R_d}\right)^2 + \frac{\rho_p g}{\rho_d \tau}}\right)\right.\\
&\left. + c_4 \sin\left(t\sqrt{\left(\frac{ck_n}{R_d}\right)^2 + \frac{\rho_p g}{\rho_d \tau}}\right)\right]
\end{aligned}
\tag{3.27}
$$

By inspection a particular solution would be $p(r,t) = p_0/\rho_p g$, where p_0 is the gas pressure on the opposite side of the diaphragm, which must match the fluid pressure under the diaphragm at the relaxed position where $u = 0$, giving a solution of the form

$$
\begin{aligned}
&u(r,t)\\
&= \frac{p_0}{\rho_p g}\\
&+ \sum_{n=1}^{\infty} J_0\left(\frac{k_n r}{R_d}\right)\left[c_3 \cos\left(t\sqrt{\left(\frac{ck_n}{R_d}\right)^2 + \frac{\rho_p g}{\rho_d \tau}}\right)\right.\\
&\left. + c_4 \sin\left(t\sqrt{\left(\frac{ck_n}{R_d}\right)^2 + \frac{\rho_p g}{\rho_d \tau}}\right)\right]
\end{aligned}
\tag{3.28}
$$

The values of c_3 and c_4 are dependent on the initial conditions selected. However for static loading we are concerned only with the steady-state value for which the initial condition is not significant and can be selected arbitrarily, as long as the trivial case of $c_3 = c_4 = 0$ is avoided. We select $c_3 = R_d$ and $c_4 = 0$ for simplicity, then divide by the diaphragm radius to give a non-dimensionalization.

$$\frac{u(r,t)}{R_d} = \frac{p_0}{\rho_p g R_d} + \sum_{n=1}^{\infty} J_0\left(\frac{k_n r}{R_d}\right) \cos\left(t\sqrt{\left(\frac{ck_n}{R_d}\right)^2 + \frac{\rho_p g}{\rho_d \tau}}\right) \tag{3.29}$$

It should be noted that $\rho_p g R_d$ has physical meaning – it is the difference in pressure at the reference datum p_0 and at the base of the tank, p_b. Considering the steady state, and non-dimensionalizing time

$$u^*(r^*) = \frac{p_0}{p_b - p_0} + \lim_{t^*\to\infty} \sum_{n=1}^{\infty} \left[J_0(k_n r^*) \cos\left(t^* \sqrt{k_n^2 + \frac{\rho_p g R_d^2}{\rho_d \tau c^2}}\right)\right] \tag{3.30}$$

In order to employ the laws of integration, we must convert the infinite summation of discrete values to one of infinitely dense infinitesimal values. To do this, a dense function of roots of the Bessel function J_0 is defined as

$$k(n) = k_{roof(n)} \quad n \in R \tag{3.31}$$

Thus,

$$
\begin{aligned}
&u^*(r^*) \\
&= \frac{p_0}{p_b - p_0} \\
&+ \lim_{t^* \to \infty} \int_0^{\infty} \left[J_0(k_n r^*) \cos\left(t^* \sqrt{k^2 + \frac{\rho_p g R_d^2}{\rho_d \tau c^2}} \right) \right] dn
\end{aligned}
\tag{3.32}
$$

It is known that the nth root of the Bessel function J_0 occurs pseudorandomly between $\pi(n-1)$ and πn. Thus

$$
\int_{n-1}^{n} k(\eta) d\eta = k_n \approx \pi\left(n - \frac{1}{2}\right) = \int_{n-1}^{n} \pi\eta d\eta \tag{3.33}
$$

This suggests that for the purposes of integration and considering sufficiently many values of n to alleviate the variation between $\pi(n-1)$ and πn, a safe approximation is given by $k(n) = n\pi$.

$$
\begin{aligned}
&u^*(r^*) \\
&= \frac{p_0}{p_b - p_0} \\
&+ \lim_{t^* \to \infty} \int_0^{\infty} \left[J_0(n\pi r^*) \cos\left(t^* \sqrt{n^2\pi^2 + \frac{\rho_p g R_d^2}{\rho_d \tau c^2}} \right) \right] dn
\end{aligned}
\tag{3.34}
$$

Or

$$
u^*(r^*) = \frac{p_0}{p_b - p_0} + h(r^*) \tag{3.35}
$$

We now have $h(r^*)$ expressed in its Hankel Transform, given by

$$H(n) = \lim_{t^* \to \infty} \left[\cos\left(t^* \sqrt{n^2\pi^2 + \frac{\rho_p g R_d^2}{\rho_d \tau c^2}} \right) \right] \tag{3.36}$$

Recalling that $c = \sqrt{\frac{\sigma}{\tau \rho_d}}$,

$$H(n) = \lim_{t^* \to \infty} \left[\cos\left(t^* \sqrt{n^2\pi^2 + \frac{\rho_p g R_d^2}{\sigma}} \right) \right] \tag{3.37}$$

Therefore the diaphragm can be readily modeled using the inverse fast Hankel transform. We also note that all oscillations of the diaphragm are governed by a single non-dimensional parameter, the Bond Number

$$Bo = \frac{\rho_p g R_d^2}{\sigma} \tag{3.38}$$

$$u^*(r^*) = H^{-1}\left\{ \lim_{t^* \to \infty} \left[\cos\left(t^* \sqrt{n^2\pi^2 + Bo} \right) \right] \right\} \tag{3.39}$$

Note that small Bond Numbers, which correspond to smaller tanks with proportionally thicker diaphragms, will result in an imaginary coefficient in the Hankel transform, and thus fewer Bessel functions contribute to the deformation and would tend to reduce oscillations and the potential for folding and rubbing.

3.3 Transient Analysis

A direct analytic analysis of a transient case would require explicitly solving the Navier-Stokes equations for pressure and substituting the result into the governing equation derived above. Since the Navier-Stokes equations cannot be solved explicitly, the set of PDEs must be solved as a system. However, since slosh exhibits some stochastic behavior, multiple solutions exist. Additionally, due to slosh resonance, a small change in input conditions could result in a discontinuity in the result. This means the problem is not well-posed, and therefore cannot be explicitly solved. Instead, a dimensional analysis will be conducted.

From the above, the controlling parameters are density, acceleration, diameter, and surface tension. In the transient case the vibration frequency will need to be added to this list. Breaking down each dimensional unit as a collection of mass (M), length (L), and time (T) base units, the following relations are obtained:

$$[\rho] = ML^{-3} \quad [g] = LT^{-2} \quad [R_d] = L \quad [\sigma] = MT^{-2} \quad [f] = T^{-1} \tag{3.40}$$

By the Buckingham Π Theorem, five governing physical properties defined in terms of three base units can be reduced to a relation among two non-dimensional groups. Thus two variables are selected as starting parameters to be non-dimensionalized by the other three; specifically, acceleration and frequency are selected.

For acceleration to have a unity exponent in the non-dimensional group $\Pi_1 = g\rho^a R_d^b \sigma^c$ with consistent units, the following relations must be satisfied:

$$M: a + c = 0 \tag{3.41}$$

$$L: 1 - 3a + b = 0$$

$$T: \ -2 - 2c = 0$$

From the time equation, $c = -1$. Then, from the mass equation, $a = 1$. Finally, from the length equation, $b = 2$. Therefore $\Pi_1 = g\rho R_d^2/\sigma$, which is simply the Bond Number, which is already known to describe the steady-state condition of the tank.

Repeating the process for the frequency, where $\Pi_2 = f\rho^a R_d^b \sigma^c$, the equations for unit consistency become:

$$M: a + c = 0$$

$$L: -3a + b = 0 \qquad (3.42)$$

$$T: \ -1 - 2c = 0$$

From the time equation it is seen that $c = -0.5$. From the mass equation it is found $a = 0.5$. Finally from the length equation, $b = 1.5$ can be calculated. Thus $\Pi_2 = (f^2\rho R_d^3\sigma^{-1})^{1/2}$. Most slosh studies consider the dominating paramters to be the Bond Number and Weber Number, which is given by $V^2\rho R_d\sigma^{-1}$. Equating these we see that $We = \Pi_2^2$ if the characteristic velocity is taken to be $V = fR_d$. Thus the second parameter of interest is taken to be a modified Weber Number for oscillating flows given by

$$We = \frac{f^2\rho R_d^3}{\sigma} \qquad (3.43)$$

3.4 Application of Non-Dimensional Numbers

Physically, the Bond Number represents the ratio of pressure forces acting to displace the surface of the fluid to the surface tension forces acting to resist deformation. In practice EDTs are used to contain hydrazine, which has a density of $\rho_p = 1010\ kg/m^3$. Sloshing concerns have predominantly existed during ground transportation and pre-launch countdown, so the acceleration due to gravity at Earth surface of $g = 9.81\ m/s^2$ is suitable. EDTs currently range in size from $120\ mm < R_d < 508\ mm$. The surface tension of pure hydrazine is $\sigma = 0.062\ N/m$. Thus the range of Bond Numbers is given by $2300 < Bo < 41240$.

The fill fraction, FF, is by itself a non-dimensional number of interest. Throughout the use of the tank it will run the full range of $0 < FF < 1$. During ground transportation and pre-launch countdown, however, the tank should be nearly full, $FF \approx 1$. For completeness, the full range will be investigated.

Finally, for the oscillating Weber Number, the frequencies excited by semi-tractor trailers during transportation on interstate highways, where the frequencies will be the highest, are highly dependent on the suspension system of the trailer. In general, however, the primary frequencies excited are less than 25 Hz, so this will be the range evaluated. This gives a maximum Weber Number of $We = 1.33 \times 10^6$ for the largest tanks.

Figure 13 shows the regimes of influence as a function of Bond Number and Weber Number. As shown, since both numbers are significantly greater than unity, capillary effects can be neglected. It is also shown that the relative dominance of inertia and gravity is given by the ratio of the Bond Number and Weber Number, known as the Froude Number. As a result, some in the literature have suggested that the individual matching of Bond Number and Weber Number is not necessary for similitude, as long as the Froude Number is matched. The derivation in Section

3.1 and Section 3.2, however, shows that the Bond Number and Weber Number dictate very different aspects of the flow, and must be treated separately in their application to EDTs.

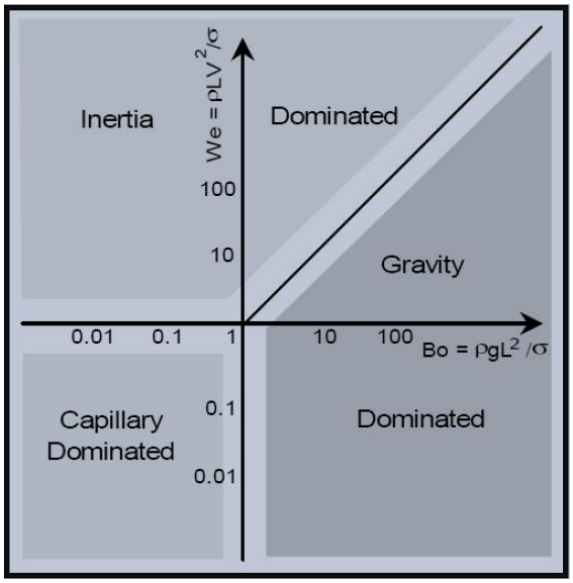

Figure 13 - Influence of Bond and Weber Numbers on Slosh Regime

As a result of their ready availability and to increase the applicability of testing to EDTs manufactured by ATK, the EDTs used for the scaled experiment will be actual production EDTs, and therefore the range of tank radii available for testing is exactly the range of in-service EDT radii. Additionally, as the experiment will be performed in a laboratory, the acceleration due to gravity will be the value at Earth's surface. Therefore, in order for the Bond Number to be matched, the fluid property ρ/σ must be matched. With this constraint set, then in order to match the Weber number the vibration frequency must also be matched. This will result in a 1:1 scaling.

Hydrazine fuel cannot be used due to its flammability. Instead, a surrogate fluid with a similar ρ/σ value must be used. The selected fluid must have strong chemical compatibility with EPDM rubber and must be safe to work with.

Surrogate fluids frequently used in propellant slosh studies include Novec, water, and fluorinert FC-72. A comparison of their fluid properties is given in Table 3. As shown, hydrazine has an unusually high surface tension, a property most closely comparable to water. Water and hydrazine also have nearly identical densities, giving a ρ/σ ratio difference of 16%. Water is extremely non-hazardous, and use in previous experimentation has demonstrated compatibility with EPDM rubber. It is thus the ideal surrogate fluid for 1:1 scale EDT testing.

Table 3 - Comparison of Surrogate Fluid Properties

	Hydrazine	**Novec**	**Water**	**FC-72**
Density (kg/m^3)	1.01×10^3	1.50×10^3	9.97×19^2	1.68×10^3
Surface Tension (N/m)	6.20×10^{-2}	1.90×10^{-2}	7.30×10^{-2}	1.00×10^{-2}
Ratio (s^2/m^3)	1.63×10^4	7.89×10^4	1.37×10^4	1.68×10^5

3.5 Chapter Summary

By considering a differential element of diaphragm it was determined that two types of forces act on the diaphragm. Edge forces occur along the perimeter of the element as a result of tension at the surface of the fluid, and consequently in the membrane material, while facial forces exist normal to the membrane as a result of hydrostatic pressure. To make the problem analytically solvable, an infinitesimally thin diaphragm is considered to eliminate the internal forces of flexural rigidity. Additionally, small angle approximations are made, requiring that the shape of the diaphragm at a steady resting condition is not a complicated geometry.

With these assumptions, a governing equation was produced using Newton's second law as a basis. The governing equation, derived in much the same way as the wave equation, is not surprisingly similar to it with an additional term to

account for the distributed pressure load. The governing equation was thus approached utilizing the same methods as would be used for the standard wave equation in cylindrical coordinates. Ultimately a complex series of Bessel functions results, but after non-dimensionalizing the solution it is found that the problem setup, including such parameters as the propellant properties and tank geometry, was preset only as a single non-dimensional parameter, the Bond number [24].

With the set of dimensional parameters responsible for the steady-state solution known, and recognizing that the only additional parameter introduced by vibrating the EDT is the frequency of oscillation, a Buckingham Π analysis was performed to determine the non-dimensional grouping associated with the frequency of oscillation. It was determined that the Weber number was this parameter, modified with a characteristic velocity based upon the oscillation frequency. Thus, as predicted by previous slosh studies, the Bond Number and Weber Number, and consequently their ratio the Froude Number, are the primary contributing factors to describing the slosh behavior of a vibrating EDT.

Chapter 4
Computational Study

In developing the analytic solution, the assumption of a taut diaphragm severely limits the practical utility of the model. To model the diaphragm as anything other than elastic will require a computational approach. The computational approach selected will couple the structural simulation of diaphragm deformation with the fluid simulation of the propellant. The model used for the fluid phase is a hydrostatic pressure distribution in the tank reference frame, while the model for the diaphragm is an inextensible cloth model commonly used in textile simulations. The inextensibility is maintained using an iterative strain-relieving algorithm based on a mesh of finite-mass elements connected by imaginary critically-damped linear springs.

4.1 Fluid Phase Simulation

The fluid phase is simulated using a hydrostatic pressure distribution, taken in the reference frame of the tank. This is as opposed the VOFequations traditionally used in slosh models. The VOF equations are ideal for open slosh flows, which are effectively multiphase in the vicinity of the gas-liquid interface. Droplets may separate from the bulk flow and traverse the gas phase, only to later recombine with the bulk fluid. In EDTs, this is not possible as the gas and liquid phases are entirely separated by a solid phase, and thus only bulk fluid exists. Additionally, since the fluid is incompressible, a control volume selected arbitrarily in the tank considered for a period of time during which the diaphragm does not enter the control volume

must experience zero net flow. Thus the bulk of the fluid can only experience flow due to local recirculation, and true fluid flow only exists in the vicinity of the diaphragm. These flow velocities are experimentally observed to be small for low-frequency oscillations, and thus the effect on static pressure is negligible compared to the effect due to the potential energy of hydrostatics.

4.1.1 Thought Experiment

To examine the hydrostatic fluid pressure distribution in a non-inertial reference frame, a thought experiment is considered to simplify the problem by eliminating fluctuating accelerations and the minor effect of local flow around the diaphragm. The thought experiment consists of a fully enclosed railroad car. At the origin, an arbitrary point selected on the ceiling of the railroad car, a massless tether is affixed, the other end of which is connected to a large point mass. The air is considered incompressible and inviscid. When the system is held stationary, the result is trivial. The mass will hang due to gravity, and will be retained due to the tether vertically. The situation becomes less trivial when the train accelerated uniformly, where the tether will form an angle with the veiling of the car. The situation is depicted in Figure 14.

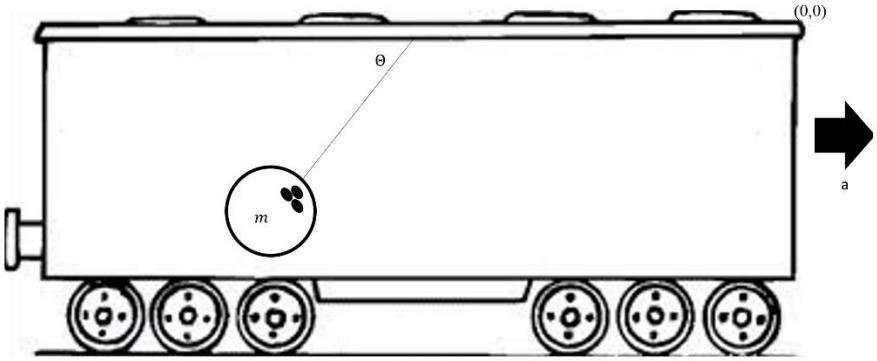

Figure 14 - Though Experiment of Pendulum in Train Car

Considering the mass as a free body, two forces act on it: a gravitational body force $m\vec{g}$ and a tension force $\vec{T}$. Evaluating a force balance in the vertical direction, $mg = T\sin\theta$. In the horizontal direction, $T\cos\theta = ma$. Combining the equations to eliminate T, $mg = ma\tan\theta$, or $\tan\theta = g/a$. Thus $\sin\theta = g/\sqrt{a^2+g^2}$. The magnitude of the tension force is $T = m\sqrt{a^2+g^2}$.

Thus, considering the reference frame of the train car, the contents experience an apparent body force at an angle of $\tan^{-1} g/a$ with an magnitude per unit mass of $\sqrt{a^2+g^2}$. The mass is now removed, and the train car is filled with water. For the stationary car, the gauge pressure is given by $p_g = -\rho g y$.

For the accelerating train car, the coordinate system is tilted. The distance between an arbitrary point (x, y) and a line passing through the origin representing an isobar, given by the relation $y = -ax/g$, is $-(ax+gy)/\sqrt{a^2+g^2}$, and the magnitude of the acceleration is $\sqrt{a^2+g^2}$. Thus the gauge pressure distribution is given by $-\rho(ax+gy)$.

4.1.2 Application to EDTs

The same basic principle applies in an accelerating EDT as it does in a train car. The primary difference is that the EDT is not necessarily filled, so the selection of the origin from which the gauge pressure is measured with respect to is no longer trivial. It is convenient to consider the origin as defined in terms of the FF for convenience of the end user, but is more closely related to the height of the free surface of the resting tank with no diaphragm. For this purpose, the first origin considered is located at the exact center of the spherical tank. Positive fluid height signifies a free surface above this point, and is normalized by the radius of the tank. By this convention, the fluid height must be in the range $-1 \leq h \leq 1$.

The volume of a spherical cap is traditionally given based on its height. To adjust to this coordinate system, the origin is placed at the bottom of the tank, with the same sign convention as previously. To denote measurements in this coordinate system, a superscript zero is used. The height of the spherical cap is then in the range $0 \leq h^0 \leq 2$, where $h^0 = h + 1$. The volume of the cap is then given by [25] in Eq. (4.1)

$$V = \frac{\pi h^0}{6}(3 + (h^0)^2) \tag{4.1}$$

Dividing by the volume of a unity radius sphere, $4\pi/3$, the FF is computed to be

$$FF = \frac{h^0}{8}(3 + (h^0)^2) = -\frac{h^3}{4} + \frac{3h}{4} + \frac{1}{2} \tag{4.2}$$

The fluid height in the center origin system is then found by taking the roots of the polynomial in Eq. (4.2) for a given FF and selecting the one in the appropriate range. The free surface will thus exist at a distance h from the center of the tank regardless of the direction of the body force. When the body force exists at a slope of g/a as determined in the thought experiment, the equation for the free surface plane becomes

$$-ax + gz + FF\sqrt{a^2 + g^2} = 0 \tag{4.3}$$

With this plane serving as a the free surface giving a new, third, origin, the distance from an arbitrary point (x, y, z) to the neutral plane is given by

$$d\left(p_g = 0, (x, y, z)\right) = \frac{-ax + gz}{\sqrt{a^2 + g^2}} + FF \tag{4.4}$$

Thus, the pressure distribution in the tank is given by fluid statics theory from [26] in Eq. (4.5).

$$p_g = \rho\left(-ax + gz + FF\sqrt{a^2 + g^2}\right) \tag{4.5}$$

Since this is now with reference to the free surface plane, along which the static pressure must equal the pressurant gas pressure, the gauge pressure computed by Eq. (4.5) is also the net pressure acting on the diaphragm at a given point accounting for the pressure on both sides of the diaphragm.

To ensure that the governing assumption, that potential energy is the dominating factor in pressure distribution, an order of magnitude study is conducted. From Bernoulli's Equation, for an incompressible, inviscid fluid, pressure can be varied due to kinetic energy per unit volume or potential energy per unit volume. For an exemplary 35 inch EDT, it is experimentally observed that the maximum fluid velocity with respect to the tank is on the order of one-quarter of the tank diameter per oscillation period. A 1 Hz pad sway test with a 12-inch center-to-peak amplitude is used as an example. The maximum acceleration is given by $A(2\pi f)^2 = 474\ in/s^2$. This gives a net body force per unit mas of $611\ in/s^2$

$$\frac{\rho g R_d}{\frac{1}{2}\rho\left(\frac{1}{4}R_d f\right)^2} = \frac{32g}{R_d f^2} = \frac{32\left(611\frac{in}{s^2}\right)}{(17.5\ in)(1\ Hz)^2} = 1118 \tag{4.6}$$

This is three orders of magnitude greater than unity, indicating that a potential energy-dominated assumption will yield 99.9% accuracy.

4.2 Structural Simulation

The diaphragm is modeled using a strain-relieving inextensibility model. As with other computational schemes, it is necessary to discretize the domain into finite elements on which the effect of finite forces can be evaluated. During execution, the grid is processed in parallel, where each node is processed in two phases. The first is an unconstrained, "free" response, where the in-plane strain of the diaphragm is unimpeded. The second phase corrects the results of the first by projecting the stretched diaphragm onto a constrain manifold representing the set of all diaphragm geometries which meet the inextensibility criteria.

4.2.1 Grid Generation

In inextensibility models, the position of each node will be manipulated to maintain a constant distance between each node and its neighbors. In a triangular mesh, this will result in three constraints placed on each node. However, each node has only three free variables, corresponding to its Cartesian coordinates. This results in zero degrees of freedom solely by virtue of the mesh, a phenomenon known as grid-locking. To alleviate this problem, it is necessary to use a quadrilateral mesh, as this imposes only two constraints on the node. Additionally, it is necessary for the mesh to be structured, so that there are defined directions along which the constraints can be imposed in computational space [27].

Numerous methods exist for projecting a quadrilateral mesh over a hemisphere, mostly developed by cartographers for displaying the Earth on a flat map. Most of these projections exhibit properties which are not desirable in computation,

including grid cells with high aspect ratio or skewness [28]. The classic azimuthal projection using latitude and longitude projection, for example, has cells of high aspect ratio in the vicinity of the north and south poles. Computational models then use an inscribed cube approach, in which each side of a cube is projected outward onto the corresponding one-sixth of a sphere. The concept is depicted in Figure 15 [29].

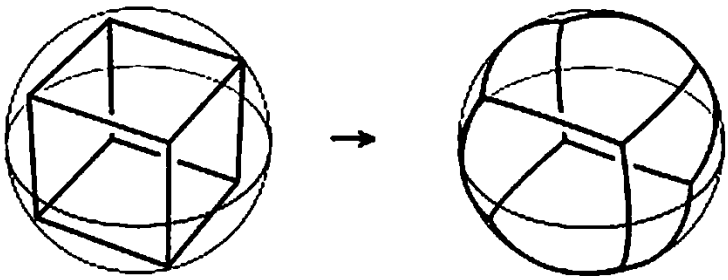

Figure 15 - Projection of a Cube onto a Sphere

Each side of the cube can be discretized into standard Cartesian grid and carried through the projection, known as a gnomonic projection. Gnomonic projections exhibit many of the desirable attributes of a computational mesh except near their interfaces, where the cells become skewed and do not necessarily form a structured mesh. Instead, only the gnomonic projection of one square onto a one-sixth sphere is considered. The lines of this mesh are then extended to form a hemisphere using a structured grid. This is depicted in Figure 16 [13].

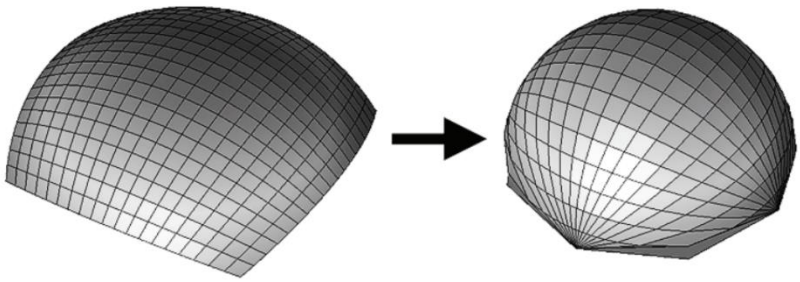

Figure 16 - Extension of One-Sixth Gnomonic Projection to Hemisphere [13]

This grid does not exhibit desirable properties, but is a structured mesh of a sphere. To resolve the problems of node clumping around the base of the hemisphere, each horizontal ring of points is considered as a group. The sequence of the points is maintained to ensure the final mesh is structured, but the x and y coordinates of each point are adjusted such that the polar angle of the points are evenly distributed. This forces the cells to become unskewed, producing the final mesh shown in Figure 17.

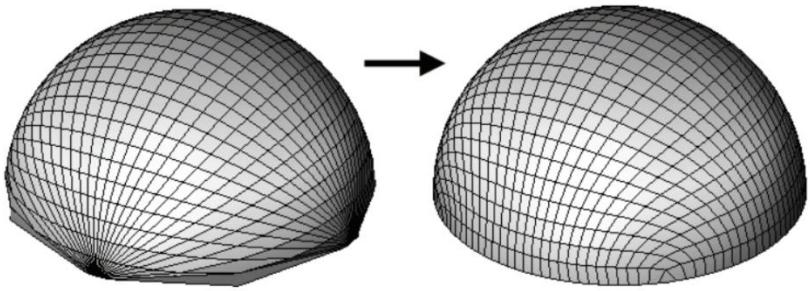

Figure 17 - Unskewing of Extended Gnomonic Projection to Final Mesh [13]

The structured grid is then represented as a square matrix. In computational space, this is a regular unit grid with standard Cartesian coordinates in two dimensions, denoted as (i, j). The geometric location of the point in space, denoted (x, y, z), is considered a point property of the node, rather than a location. Thus, although the diaphragm is plotted in physical space for rendering, it is best to visualize the mesh as a square, two-dimensional grid.

To apply boundary conditions, the support type is considered to be simply supported around the entire circumference of the diaphragm.This is taken as a Dirichlet boundary condition for all exterior notes of the mesh. To maintain this rigidity, the node masses are set to infinity. This ensures that the kinematic equations cannot impose an acceleration on these nodes, regardless of the force applied to them.

4.2.2 Unconstrained Diaphragm Response

Neglecting all internal forces of the diaphragm, two categories of external loads exist. Surface forces, which physically represent the pressure of the fluid phase, and body forces, physically representing gravity. No point forces are considered, so this constitutes all external loads. Pressure is taken to act normal to the surface.

In addition, those internal forces that are not constraints are considered. These spring relaxation forces apply due to bending strain, and are a function of the material flexural rigidity. This is taken to be a linear spring restorative force with a stiffness given by [30] in Eq. (4.7), where L represents the undeformed distance between the two outer nodes of a three-node beam.

$$k_{eq} = \frac{48\kappa}{L^2} \tag{4.7}$$

The force of the spring is taken in the direction normal to the surface and applied to the node in the center of the three-node beam. The spring is critically damped, which decreases the effective force of the spring due to dynamic effects. The correction is given in Eq. (4.8), where δ is the out-of-plane displacement of the center node of the three-node beam.

$$F_b = k_{eq}\delta - 2\vec{v}\sqrt{mk_{eq}} \tag{4.8}$$

The implementation of this algorithm is shown in Listing 1.

Listing 1 - Bending Force Spring Relaxation

```
function [Fbx,Fby,Fbz,keq] =
InternalForces(X,Y,Z,Rest,kappa,NX,NY,NZ,ioff,joff)
    X2 = circshift(X,[-ioff -joff]);
    Y2 = circshift(Y,[-ioff -joff]);
    Z2 = circshift(Z,[-ioff -joff]);
    XM = circshift(X,[-ioff/2 -joff/2]);
    YM = circshift(Y,[-ioff/2 -joff/2]);
    ZM = circshift(Z,[-ioff/2 -joff/2]);
    NXM = circshift(NX,[-ioff/2 -joff/2]);
    NYM = circshift(NY,[-ioff/2 -joff/2]);
    NZM = circshift(NZ,[-ioff/2 -joff/2]);
    XC = (X+X2)/2; YC = (Y+Y2)/2; ZC = (Z+Z2)/2;
    XD=X2-X; YD=Y2-Y; ZD=Z2-Z;
    deltalength = sqrt(XD.^2 + YD.^2 + ZD.^2);
    d = abs(real(sqrt((Rest./2).^2 - (deltalength./2).^2)));
    Keq = 48*kappa./Rest.^2;
    signX = sign(abs(sqrt((XM-(XC+NXM)).^2+(YM-(YC+NYM)).^2+(ZM-
(ZC+NZM)).^2))-abs(sqrt((XM-(XC-NXM)).^2+(YM-(YC-NYM)).^2+(ZM-
(ZC-NZM)).^2)));
    Fb = signX.*d*Keq;
    Fbx = Fb.*NXM; Fby = Fb.*NYM; Fbz = Fb.*NZM;
    Fbx = circshift(Fbx,[ioff/2 joff/2]);
    Fby = circshift(Fby,[ioff/2 joff/2]);
    Fbz = circshift(Fbz,[ioff/2 joff/2]);


end
```

Once the forces acting on a diaphragm element are known, they are summed. Newton's second law is used to compute the acceleration of each node; a first-order forward Euler approximation is used to integrate the acceleration twice to obtain

the change in position of each node. The code for this algorithm is given in Listing 2.

Listing 2 - Computation of Unconstrained Response

```
%% Compute pressure
if converged==1
    accel=-(Frequency^2)*Amplitude*sin(Frequency*t);
end
Pressure=rho*(accel*X+gravity*Z-
FluidHeight*sqrt(accel^2+gravity^2));
[NX,NY,NZ] = surfnorm(X,Y,Z);
[NodeArea] = FindNodeArea(X,Y,Z,GridSize);
%% Compute unconstrained response
 [FbX,FbY,FbZ,kfd] =
InternalForces(X,Y,Z,LengthXB,kappa,NX,NY,NZ,2,0)+InternalForces(
X,Y,Z,LengthYB,kappa,NX,NY,NZ,0,2);
c=2*(M.*kfd).^0.5;
FX=FbX+NodeArea.*Pressure.*NX-c.*vX;
FY=FbY+NodeArea.*Pressure.*NY-c.*vY;
FZ=FbZ+NodeArea.*Pressure.*NZ+M*gravity-c.*vZ;
%% Kinematic effect of unconstrained forces
aX=FX.*Minv; aY=FY.*Minv; aZ=FZ.*Minv;
vX=vX+aX*dt; vY=vY+aY*dt; vZ=vZ+aZ*dt;
X=X+vX*dt; Y=Y+vY*dt; Z=Z+vZ*dt;
```

4.2.3 Inextensibility Constraints

The freely deformed diaphragm is projected into the constraint manifold using a strain-relieving approach. Each node is associated with the eight neighboring nodes, the distance between which must be returned to its initial resting value. To ensure that each pair of neighbors is considered only once, four of the neighbors are selected as fixed with respect to each node of interest. The four are selected arbitrarily, but such that the opposite pairing is not evaluated to avoid duplication. These four constraints are firm; that is, the error resulting from unrelieved strain is

computed and the process repeated until this strain is reduced below a user-definable threshold. In addition, two nodes are selected further from the node of interest and the strain between them relieved in order to dampen sharp bending, which physically represents the flexural rigidity of the EDT. For these cases, the strain is relieved with each timestep, but is not driven to zero. A mapping of the relevant neighboring points for a given point of interest is depicted in Figure 18.

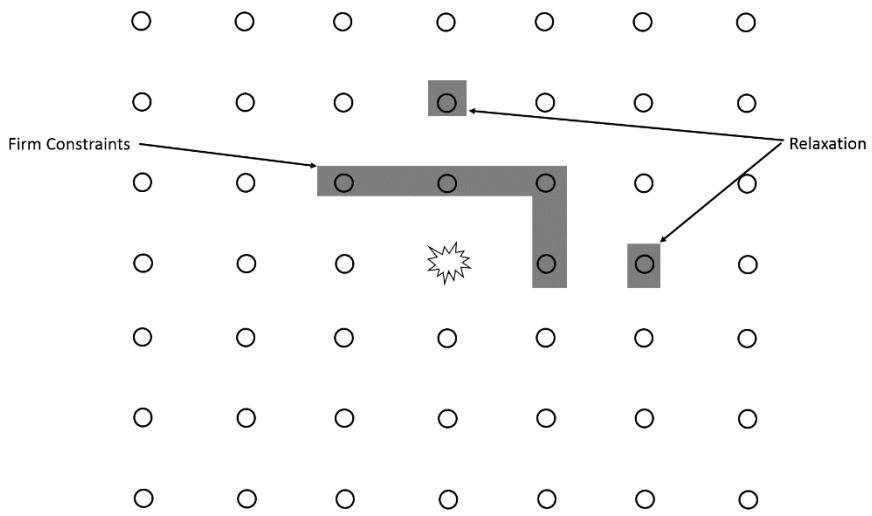

Figure 18 - Nodes of Interest Surrounding an Arbitrary Internal Node

A number of strain-limiting approaches can be taken. Histories of various algorithms and their efficiencies are detailed in [27],[31],[32],[33],[34]. The general principles for each are the same, treating each node pairing as a spring and iterating to relieve strain, thus projecting the node cloud to the constraint manifold. The restorative force applied to a pair of nodes to return them to their rest state is taken to be proportional to the distance they have been displaced from their rest separation. This is based on Hooke's Law, where the diaphragm material between any pair of nodes is taken to behave like an ideal linear spring. The direction of the displacement each node is subjected to is considered to be along the axis of the line connecting the two nodes. The proportion of the motion which is assigned to each

node is based on the portion of the mass of the two particles taken by the particle moving.

The algorithm is implemented as a subroutine. Several parameters are needed in order to perform the computation. First, `X`, `Y`, and `Z` are read in. These matrices, indexed by computational space coordinate `i` and `j`, represent the physical Cartesian coordinates of a given node. `MF` is a mass fraction, also indexed in computational space, which represents the ratio of the mass of a node to the sum of the mass of the two node system. This could be read in as the mass array itself, but the mass fraction array is constant throughout the simulation, and thus can be used for computational efficiency. `Rest` is an array of the resting length which existed between the indexed node and the offset node of interest, which is determined when the grid is created. Then, at each timestep, the node distances are forced back to these values to avoid accumulation of strain. Finally, `ioff` and `joff` are offset coordinates, measured from the indexed point, which represent the location of the second node of interest.

In order to batch process the data to enable parallelism, it is first necessary to compute the Cartesian coordinates of the second, offset point. This is done by shifting the indices of the `X`, `Y`, and `Z` matrices by the offsets `ioff` and `joff`. Next, the Cartesian coordinates of the two points are subtracted to yield a position vector of one point with respect to the other. The length of this displacement is computed, and compared to the original resting length to determine the strain, and consequently the restorative force. The strain is tracked among all points to ensure the convergence criteria is met. The error is then multiplied by the mass fraction of each particle to determine the magnitude each particle must be displaced. This is then multiplied by a unit vector along the axis of the line connecting the particles. The displacement to be applied to the second particle is then index-shifted back to

its original computational coordinates, and the displacements are applied to the spatial Cartesian coordinates. The entire process is demonstrated in Listing 3.

Listing 3 - Constrain every point to a Neighboring Point Defined by an Offset

```
function [X, Y, Z, errors] =
ConstrainToPoint(X,Y,Z,MFB,MFF,Rest,ioff,joff)
    X2 = circshift(X,[-ioff -joff]);
    Y2 = circshift(Y,[-ioff -joff]);
    Z2 = circshift(Z,[-ioff -joff]);
    XD=X2-X; YD=Y2-Y; ZD=Z2-Z;
    deltalength = sqrt(XD.^2 + YD.^2 + ZD.^2);
    error = deltalength-Rest;
    errors=sum(sum(abs(error)));
    multA=error.*MFB./deltalength;
    multS=error.*MFF./deltalength;
    xA=XD.*multA;
    yA=YD.*multA;
    zA=ZD.*multA;
    xS=XD.*multS;
    yS=YD.*multS;
    zS=ZD.*multS;
    xS = circshift(xS,[ioff joff]);
    yS = circshift(yS,[ioff joff]);
    zS = circshift(zS,[ioff joff]);
    X = X + xA-xS;
    Y = Y + yA-yS;
    Z = Z + zA-zS;
end
```

To construct the rest length and mass fraction arrays used for the inextensibility model, the undeformed grid must be mapped. The length is computed the same way, except it is stored for later use rather than used immediately. The mass fractions are computed from the input `Minv`, which corresponds to the inverse of the mass at each point. To account for rigid particles, the mass fractions of any

points assigned as rigid must be set to zero, representing infinite mass. Additionally, any point around the edge of the grid which does not have the neighbor of interest is also considered to have infinite mass, even if they are not rigid. The code associated with this mapping is shown in Listing 4.

Listing 4 - Resting Grid Length Mapping and Mass Fraction Calculation

```
function [Length,MFB,MFF] =
GridLengthMap(X,Y,Z,GridSize,Minv,ioff,joff)
    X2 = circshift(X,[-ioff -joff]);
    Y2 = circshift(Y,[-ioff -joff]);
    Z2 = circshift(Z,[-ioff -joff]);
    Minv2 = circshift(Minv,[-ioff -joff]);
    XD=X2-X; YD=Y2-Y; ZD=Z2-Z;
    Length=sqrt(XD.^2 + YD.^2 + ZD.^2);
    MFB = Minv./(Minv+Minv2);
    MFF = Minv2./(Minv+Minv2);
    MF(isnan(MF))=0;
    if ioff<0
        MF(1:-ioff,:)=0;
    else
        if ioff>0
            MFB(GridSize+1-ioff:GridSize,:)=0;
            MFF(GridSize+1-ioff:GridSize,:)=0;
        end
    end
    if joff<0
        MF(:,1:joff)=0;
    else
        if joff>0
            MFB(:,GridSize+1-joff:GridSize)=0;
            MFF(:,GridSize+1-joff:GridSize)=0;
        end
    end
```

```
end
```

4.2.4 Parallelization

To maximize the efficiency of the simulation, parallelism has been employed wherever feasible. MATLAB commands which lend themselves to parallelization are natively implemented using `parfor` loops, and any necessary additional loops have been manually declared as `parfor` types. For such a loop to be implemented, each iteration of the loop may only access or store data to a matrix's `(i,j)` coordinate. The loop must also be relatively simple, performing an identical set of operations on each iteration. To accommodate this, boundary nodes have been treate as having infinite mass so that they can be handled the same as internal nodes without being moved. The repeated use of `circshift` is also to facilitate this requirement. This allows the Cartesian coordinate matrices to be shifted such that only the `(i,j)` nodes are accessed, but the Cartesian coordinates of offset points can still be used in the algorithm.The `circfhift` function itself is implemented in a parallel method internally to MATLAB.

When a script implements parallel code through `parfor` loops, either explicitly or implicitly through built-in MATLAB commands, each iteration of the loop is constructed with a corresponding set of `(i,j)` coordinates hard-coded within. Each variant of the loop is that dispatched to a MATLAB helper program to execute and return the results. Because of the restrictions imposed on `parfor` loops, the execution of each iteration will not interfere with the others, regardless of the order in which they are executed. A collection of helper programs can be established by opening a MATLAB pool, which manages the information flow to several helper programs. As many helper programs are established as there are computational cores of the host computer, thus enabling each core to run simultaneously until the entire mesh is solved. This process has enabled the

computational time for most simulations to be on the order of 60 to 80 minutes when executed on a 64-core server.

4.3 Results

The computational simulation was tested for a variety of realistic test cases with variable EDT diameters and fill fractions to modify the Bond Number and variable oscillation frequencies and amplitudes to modify the Weber Number. Limited experimental data is available for sinusoidal oscillations of EDTs, all of which is qualitative, but comparisons are made where possible.

The first test was conducted to qualitatively observe that a transient steady state of fluid oscillation is reached. The final timestep of the oscillation should match the first timestep of thefollowing oscillation, but qualitative observation is used to ensure smoothness of the transition, indicative of matched velocities and accelerations as well as positions. The test was conducted using the parameters given in Table 4.

Table 4 - Input Parameters for Transient Convergence Test

Property	Value
Timestep	0.001 s
Mesh Cells	26×26
Allowable Strain	1%
EDT Radius	0.4445 m
Diaphragm Thickness	0.001778 m
Diaphragm Density	1070 kg/m^3
Modulus of Elasticity	8.6×10^6 N/m^2
Fluid Density	1000 kg/m^3
Fill Fraction	20%
Frequency	1 Hz
Amplitude (center-to-peak)	0.25 m

In the “peak” positions, where the magnitude of displacement is at a maximum, and thusly the body force in the tank reference frame is also at a maximum, the fluid is pressed to one side of the tank and creates a simple geometry. In the central position, where the body force is a minimum and fluid inertia is at a maximum, the fluid is dispersed unevenly along the bottom of the tank with a complex time-variant geometry. This is consistent with experimental observation.

Based on this observation, to give the best chance of a well-behaved transition from one oscillation to the next when exporting data, oscillations are considered to start and end at one of the peak positions where the fluid is more well-behaved. Taking a single oscillation starting and ending at a peak and exporting the results as a video played on loop, The reults showed the expected smooth transition from one oscillation to the next with consistent behavior after only a few oscillations. Ten

oscillations were used for all future tests to ensure complete convergence. The results of this simulation are given in Figure 19.

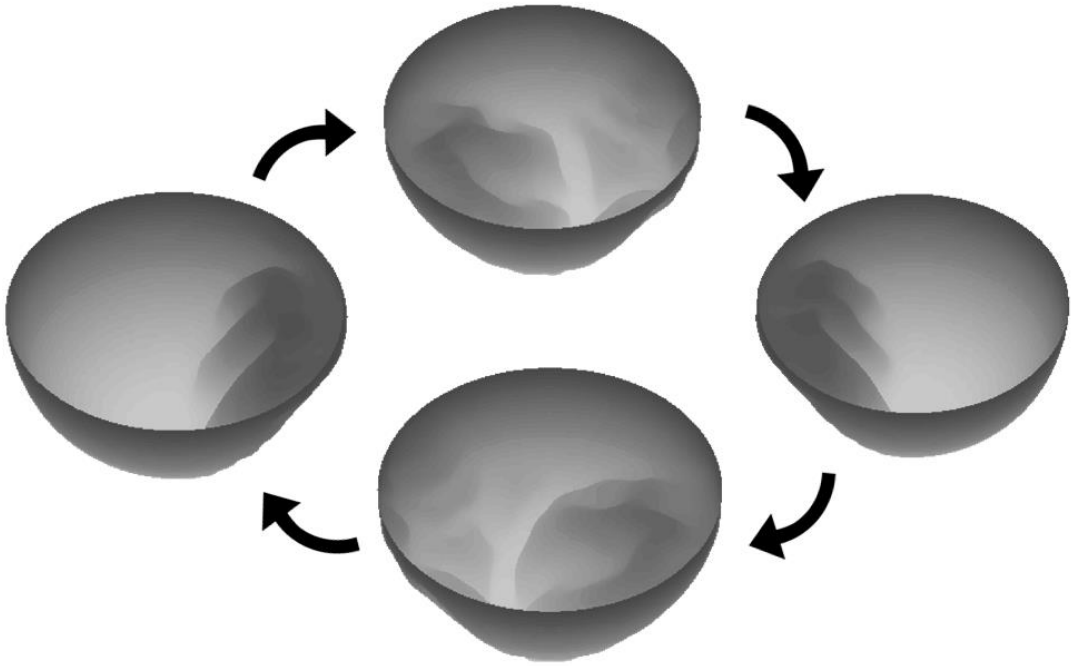

Figure 19 - Simulation Results for a 35" EDT oscillating at 2 Hz with a 25cm Amplitude and 20% FF

Next, with the results properly converged, it became pertinent to compare the computational results with experimental data. The input parameters used for this test, to be consistent with the parameters of the experiment, are given in Table 5.

Table 5 - Input Parameters for Comparison to Pad Sway Test

Property	Value
Timestep	0.001 s
Mesh Cells	26×26
Allowable Strain	1%
EDT Radius	0.4445 m
Diaphragm Thickness	0.001778 m
Diaphragm Density	1070 kg/m^3
Modulus of Elasticity	8.6×10^6 N/m^2
Fluid Density	1000 kg/m^3
Fill Fraction	80%
Frequency	1.25 Hz
Amplitude (center-to-peak)	0.25 m

For the experiment, a 35 inch EDT was fitted to an oscillating shake table and filled to 80% FF. No quantitative data was collected, only video capturing the slosh event for comparison to rendered computational results. The EDT utilized is not perfectly spherical, which will introduce minute error, but nevertheless allows a qualitative comparison. Shown in Figure 20 is a side-by-side comparison of a the computational and experimental videos, each taken on the 17^{th} frame of a 24-frame oscillation at 30 frames per second.

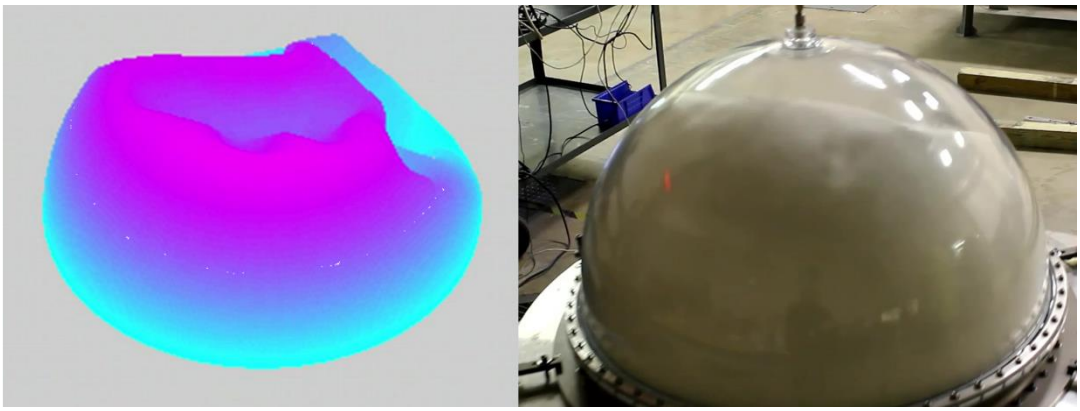

Figure 20 - Comparison of Computational Results to Pad Sway Experiment with 35" EDT at 1.25 Hz with 80% FF

As shown, there is strong correlation between the simulation and experimental video. The vertical displacement of the fluid on the near side of the tank is consistent, as are the locations of folds and ridges. The small crater at the top of the dome is also a feature of both topologies. The test shows that, on a qualitative level, the simulation is an accurate predictor of experimental reality, a sign that the various assumptions of inextensibility, linear spring flexural rigidity, and potential energy dominated flow, are all valid assumptions.

It was observed during the pad sway test comparison that the simulation ridges do not match the experimental folds in appearance. The simulation ridges are steeper but smoothed at their peaks in comparison to experimental data. This is not an indication of a faulty assumption, but rather a mismatch between the flexural rigidities of the material. This is likely due to the dependence of the flexural rigidity on the modulus of elasticity, which is not necessarily constant for a hyperelastic material. The assumed value of 8.6 MPa is based on material testing conducted by ATK, but is only an average along the pre-failure stress-strain curve of AF-E-332. To determine how this might be impacting the ridges, a numerical study was conducted in which the modulus of elasticity was varied from half of the

averaged value to double the averaged value. The experiment was conducted at 1 Hz. All other properties are held constant from the pad sway test.

The results of the comparison are shown in Figure 21. It is clear that the lower modulus of elasticity, also corresponding to a lower flexural rigidity, exhibits the desired behavior of shallower and steadier ridges, consistent with the experimental video.

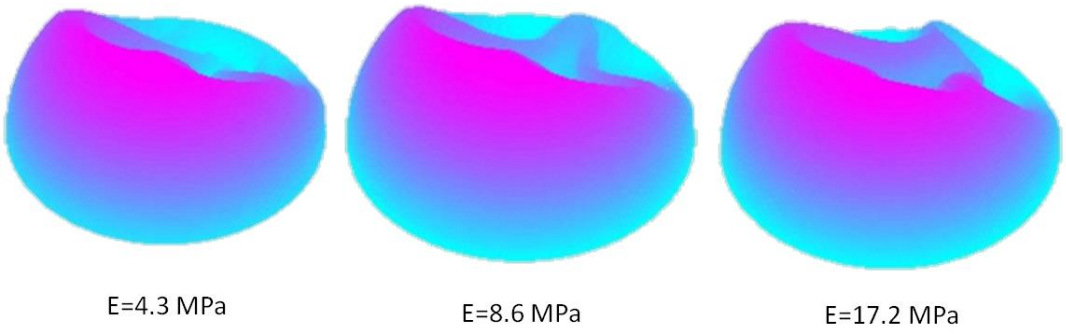

Figure 21 - Comparison of Deformation for Various Moduli of Elasticity

This indicates that the average modulus of elasticity experienced in the diaphragm is lower than the average for the entire stress-strain curve. The reason for this is depicted in Figure 22, where it can be seen that hyperelastic materials exhibit lower-than-average elasticity in mid-range deformation regimes [35].

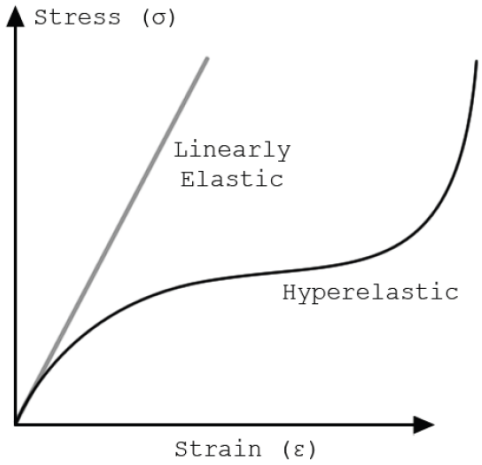

Figure 22 - Comparison of Linear and Hyperelastic Stress-Strain Response[35]

4.4 Chapter Summary

To computationally model the diaphragm motion, the problem was divided into an isolated fluid phase and structure phase. The fluid phase was analyzed for the primary influential factors, through which it was determined that hydrostatic forces in the tank reference frame, a combined effect of the forced oscillation motion and gravity, yield a very accurate pressure distribution for application to EDTs without the need to dynamically mesh the fluid volume and computationally solve using the discretized VOF equations, which is a mathematically intense task.

The unconstrained membrane was modeled using a free-body approach for each node. The forces considered included a body force representing gravity, the net pressure term from the fluid phase simulation, and a spring force taken normal to the surface at each node intended to dampen bending of the three-node beam centered on the node of interest based on the flexural rigidity of the diaphragm.

These forces were then applied to the node to compute an unconstrained acceleration and numerically integrated to obtain node positions.

The node positions were then slowly projected towards a constraint manifold to limit the in-plane strain between adjacent nodes to maintain the inextensibility of the material. This is again accomplished using a linear spring model until the total strain on a node is reduced below a specified threshold. This inextensibility assumption has been shown to be consistent with experimental observation.

Several tests were conducted of the computational model. The first demonstrated that dynamic convergence is achieved rapidly and is consistent with expected appearance. Another test was conducted to demonstrate consistency with experimental observations at a qualitative level, which was successfully achieved. Some deviations were observed that were attributed to an incorrect modulus of elasticity. Numerical experiments confirmed that a lower modulus of elasticity yields more consistent results.

Chapter 5
Experimental Analysis

To experimentally validate the analytic and computational models, consequently improving confidence in the model, it is necessary to instrument an EDT such that the diaphragm shape can be experimentally captured. Such measurements can be taken using optics or tactile feedback, but tactile measurement such as utilized in Coordinate-Measuring Machines would be difficult to implement due to the presence of the solid tank shell containing the pressurant gas. To accommodate optical measurements, a modified EDT containing an acrylic tank shell, rather than the traditional titanium, was provided by the tank manufacturer. The tank is otherwise identical to flight-ready EDTs and was manufactured by the same production line. The experiment consists of using optical instrumentation to map the three-dimensional diaphragm shape for a static tank at various FF values, which will be used for comparison to analytic and computational predictions.

5.1 Stereoscopic Imaging Theory

Human beings perceive objects to be at a given depth by analyzing the differences in the images perceived by each eye. An object which is far away is essentially identical to both eyes; the small separation, on the order of a few inches, is small compared to the distance to the object. For closer objects, the distance between the eyes becomes less negligible, and thus each eye will see a slight shift in the location of the image. The brain can see this shift and interpret it as depth information. Most three-dimensional optical instrumentation is based on this

premise, where an image captured from two cameras in relatively close proximity can be used to fully describe a depth field.

This method, though adapted from a biological concept, has the potential to yield inaccurate results when applied to the current application. When similar objects are placed in our field of vision such that both eyes see a pattern of many apparently identical objects, it is no longer possible to pair the object as seen in each eye's image. Two identical objects next to each other could produce the same pair of images as two objects of different size positioned at different depths. This situation does not bother humans in daily situations, as the brain attempts to fill in missing information based upon best guesses. This can, however, result in an incorrect perception of the situation, which is the fundamental technique used by optical illusions to cause the brain to perceive something other than the truth.

For an experimental optical instrumentation technique, it is necessary to overcome this problem, as different pieces of the diaphragm will of course appear similar and could result in ambiguities. To accomplish this, different elements of the field must be marked in some uniquely identifying way. This can be accomplished by projecting a small image onto different areas of the object in a grid, where each grid cell is identified by a unique image. The cameras can then identify this unique image, and use it to associate portions of a captured image from multiple cameras. In fact, the source of projection could itself be used in place of a camera, since the original image is entirely known from the perspective of the projector; it is simply the grid that is being projected. Thus all that is needed is the projector and a single camera. As depicted in Figure 23, a single camera perspective will see shifts in the individual grid locations produced by the projector, which can be used to indicate depth. A plot of the displacement of a grid cell against the location at which the grid cell would appear if viewing a distant flat wall is then an accurate depth map of the field of view.

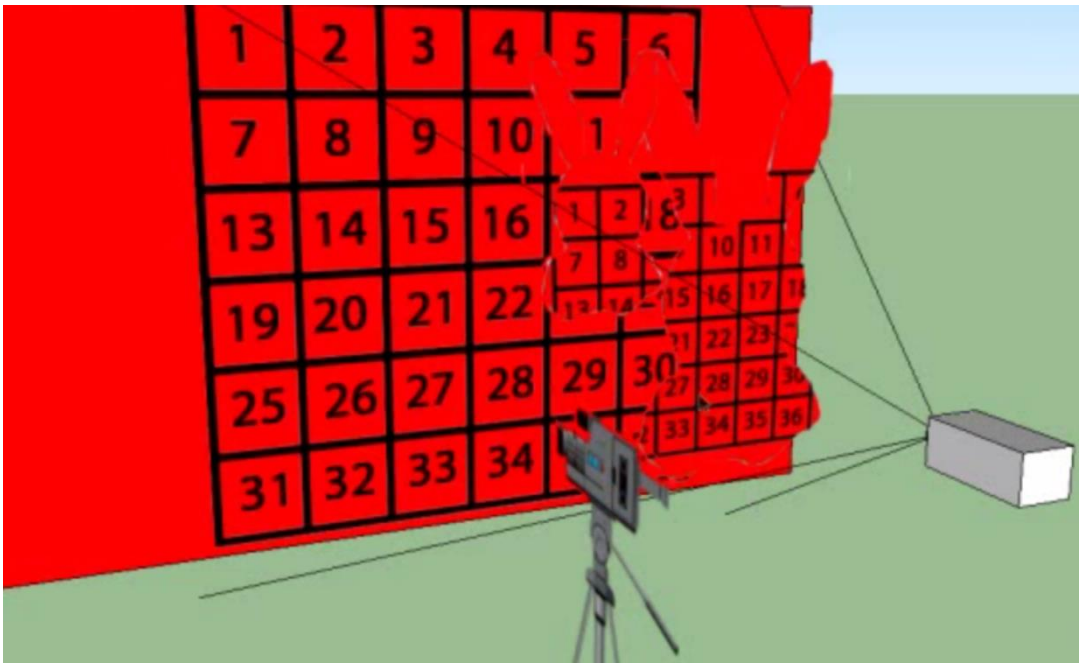

Figure 23 - Rectangular Grid Projected onto a Surface and Viewed from an Angle

To avoid confusion between the images used for marking and identifying an object and images that naturally occur in the field of view, the markers utilized must be of a wavelength not otherwise present in the image, or at least present uniformly. For this reason, a single frequency of infrared light is used to mark the grid locations. In Figure 23 the unique marking frequency is denoted in black, while all other frequencies have been cast to red [36].

In practice, for reasons of spatial resolution, it is not desirable to actually project numbered cells on to the object, but rather to use a constellation approach, in which a pattern of dots reminiscent of the night sky is projected. Unique patterns observed by the camera like constellations can then be correlated to their original position in the projected image, just as sailors used astronomy to navigate open waters before the invention of the Global Positioning System.

When a Liquid Crystal Display (LCD) projector is used on flat wall from an oblique angle, the resulting image is deformed into a quadrilateral, often beyond

recognition. The problem, known as keystone due to the similarity in shape of the deformed rectangle to the load-bearing stone of ancient roman arches, is also present in the projection of the constellation grid onto an object for scanning. While an LCD projector can be adjusted based on its position relative to the flat wall, the geometry of the surface is unknown in a scanning application, so the image cannot be corrected. For this reason, the constellation must be mathematically generated in such a way that if a small portion of the star field is deformed by keystone, it is still uniquely distinguishable from any other constellation in the field. An example of such a star field is depicted in Figure 24. Where a discontinuous jump takes place in the star field, such as at the edge of an object, the camera will fail to observe some of the original constellations, and new star patterns will appear that don't correspond to the original projected image. Where this occurs, the new constellations must be ignored.

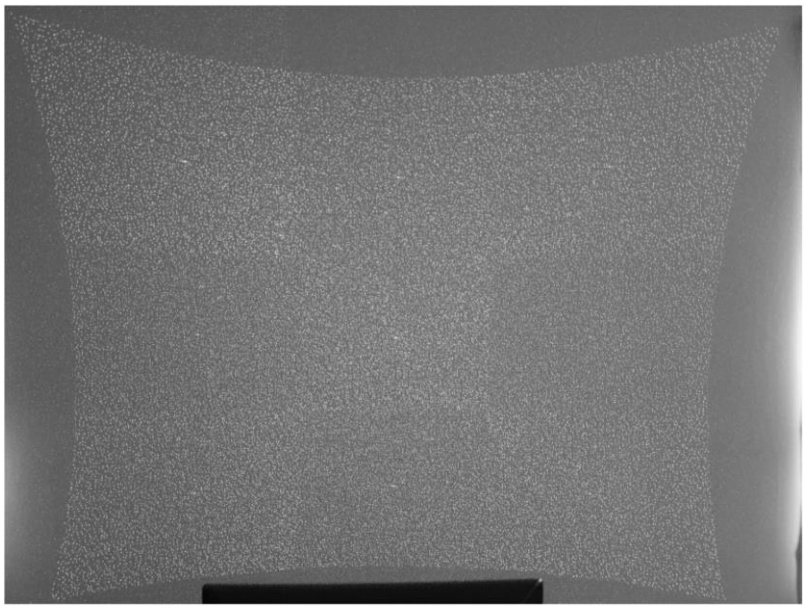

Figure 24 - Constellation Pattern of the Xbox Kinect

This arrangement appears at first glance to be a desirable instrumentation system. An infrared star field projector and a filtered infrared camera must be held rigidly a

known distance apart, and a relatively simple pattern recognition algorithm developed to compute the distance between a constellation's actual and undisturbed locations. A package containing these elements is available in the commercially manufactured Xbox Kinect, along with a visible light camera for color detection. The arrangement is depicted in Figure 25.

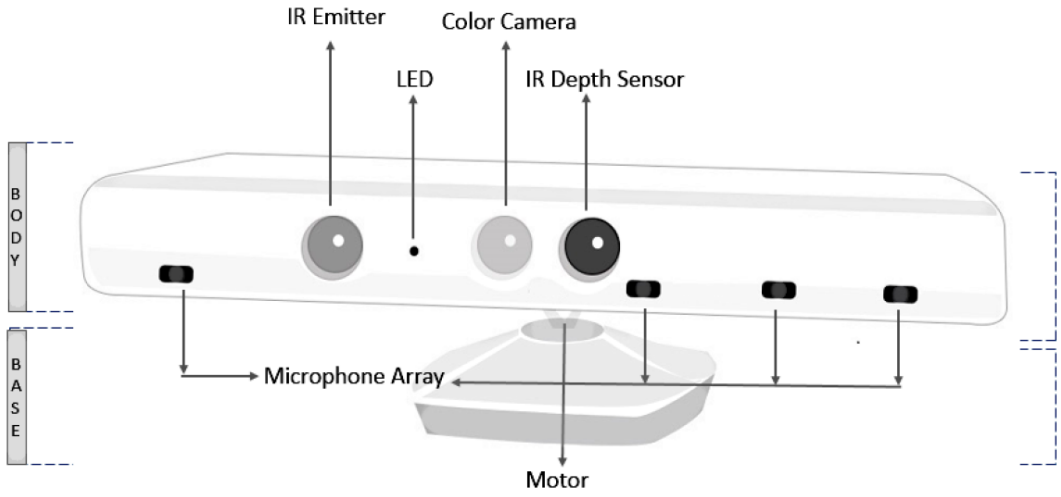

Figure 25 - Components of the Xbox Kinect

The Xbox Kinect suffers from drawbacks in three-dimensional scanning applications that were not relevant to its intended usage in video games. Notably, it suffers from an inability to perceive positions that are obscured to either the infrared emitter or sensor; for a point to be detected it must be visible to both units. To attempt to combat this problem, multiple Xbox Kinects must be used and strategically positioned so that as much as possible of the object is visible to at least one Xbox Kinect. Additionally, the relative locations and orientations of the individual units must be known from a prior alignment scan. A central computer can then be used to map the depth fields produced by each unit on a common grid with a shared origin and coordinate system. Similarities among the scans are then used to merge the surface meshes together to form a single object from the multiple

scans, ideally eliminating any blind spots. The arrangement of six units around the tank for this purpose is depicted in Figure 26.

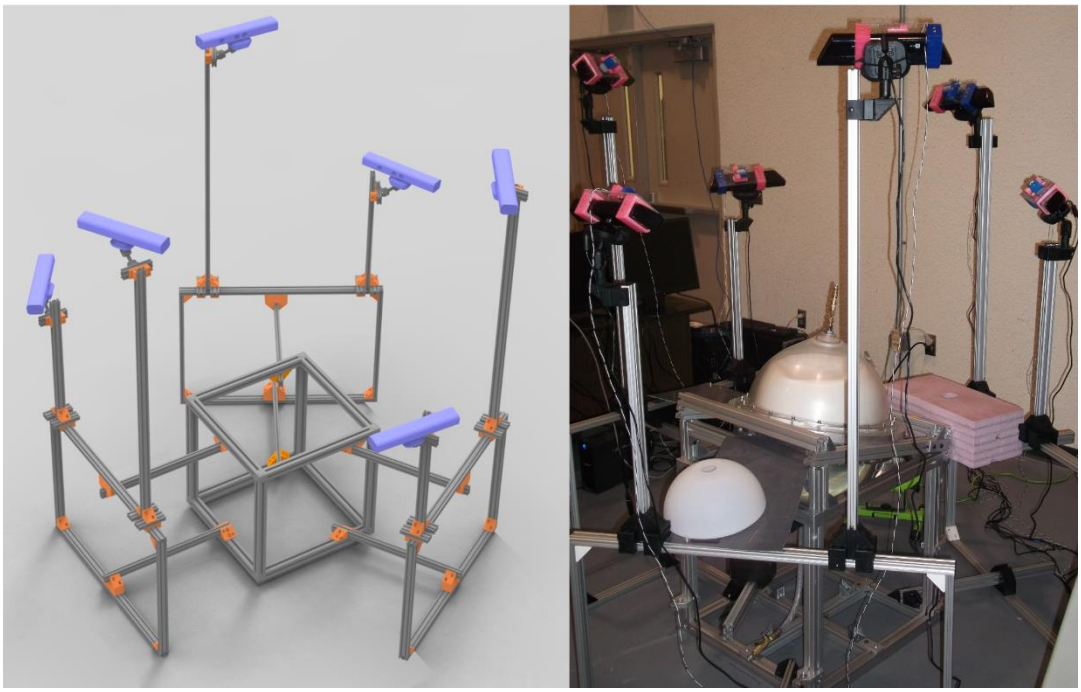

Figure 26 - Arrangement of Xbox Kinects Around EDT

5.2 Utilization of Multiple Depth Sensors

For consistency of operation among multiple units, Xbox Kinects are manufactured identically. All use the same mathematically generated star field and the same frequency of infrared light for their emitters and detectors. Thus, when multiple Xbox Kinects are operated within the same vicinity, the star fields begin to interfere. Where the stars intermesh, the algorithm sees constellations that do not correspond to any location in the original projected image. Since this is known to occur near depth discontinuities, the algorithm is programmed to ignore such constellations. This forces the rejection of most of the star field, causing a very

incomplete mesh. An ideal solution would be to utilize a unique infrared light frequency for each Xbox Kinect, but they cannot be modified in this manner.

For the purposes of this static scanning application, it is sufficient to take the scans from each Xbox Kinect in sequence rather than simultaneously. However, future studies to experimentally validate the transient diaphragm response of an oscillating tank require the solution of this issue. If different frequencies of light cannot be used, an alternative is to shake each of the Xbox Kinects using a vibrating motor. Since the emitter and detector are within the same housing, they will vibrate together and the star field associated with a given unit will be clearly visible. If each unit is vibrated differently, however, the star fields of the other units will be blurred and readily rejected. To maintain consistency of readings, it is desirable to use a common frequency, and thus the discrepancy is achieved by running the vibration motors out of phase with one another. Laboratory testing found this method to be highly successful, but individual triggering of each unit was still found to produce less image noise [37],[38].

While the issue of interference among multiple Xbox Kinect units is not an immediate problem for the current work, other difficulties arise in the use of multiple units. Each unit includes a four microphone array and two cameras: one infrared and one visible light. Additionally, there is a stepper motor used to tilt the device. All of these devices are interfaced to the host computer via a single Universal Serial Bus (USB) 2.0 connection. Considering only the image streams, the color video is sent at a resolution of 640×480 pixels, while the depth field is sent at a resolution of 320×240 pixels. Combined, this represents 384,000 pixels that must be sent for every frame sampled. As the Xbox Kinect operates at 30 Frames Per Section (FPS), this is a stream rate of 11,520,000 pixels per second. Each pixel is represented by 3 Bytes (24-bit color), where each byte represents a primary color for the color image stream. This gives a data rate of 34,560,000 bit/s,

or 32.96 MB/s. Bus access limits of the USB 2.0 standard limit its usable data rate to 35 MB/s. Thus a single Xbox Kinect is sufficient to maximize the utilization of a USB Root Hub Controller [39].

To accommodate this data rate, a separate USB Root Hub Controller must be installed in the host computer for each Xbox Kinect using a Peripheral Component Interface Express (PCIe) connection. Limitations on the number of PCIe devices which can be managed by the motherboard then impose a limit of three Xbox Kinect units. As the avoidance of blind spots necessitated six camera angles, it is necessary to utilize two motherboards connected via a simple intranet using an Ethernet switch. While commands can be issued over the Ethernet network to provide a single user interface from the primary motherboard, the 100 Mb/s speed of Cat5e cable is insufficient for the data to be shared in real-time [39].

5.3 Results

A number of samples were recorded with the scanning system. Known geometries were scanned to ascertain the reliability and accuracy of the scanning method, followed by actual EDTs will known FFs. Additionally, the center of gravity positions predicted by the scanned image of the tank were compared to the measured center of gravity position using an linear voltage displacement transducer balance board.

5.3.1 Validation Tests

Based on the resolution of the Xbox Kinect, the accuracy of the scanning system was predicted to be less than 1 mm. Scans of arbitrary geometries confirmed that the mean distance between vertices was 0.8 mm. To confirm this, two known

geometries representative of realistic diaphragms were 3D printed using polylactic acid, then scanned using the Kinects for comparison.

The first model scanned was representative of a mid-range fill fraction. The scanned model was reoriented and aligned with the CAD model of the original geometry used to print the test article. At each XY location, the distance between the Z coordinates was measured. Various statistical analyses were performed on this data, which are summarized in Table 6. An overlay comparison of the two models demonstrating the conformance of the scan is shown inm Figure 27.

Table 6 - Difference Between 3-D Printed Model and Scanned Model (Short)

Avg. Z_{diff} (mm)	Standard Deviation (mm)	Avg. Euclidean Distance (mm)	Min. Euclidean Distance (mm)	Max. Euclidean Distance (mm)
-1.418	5.1836	2.9999	0.0000	53.2923

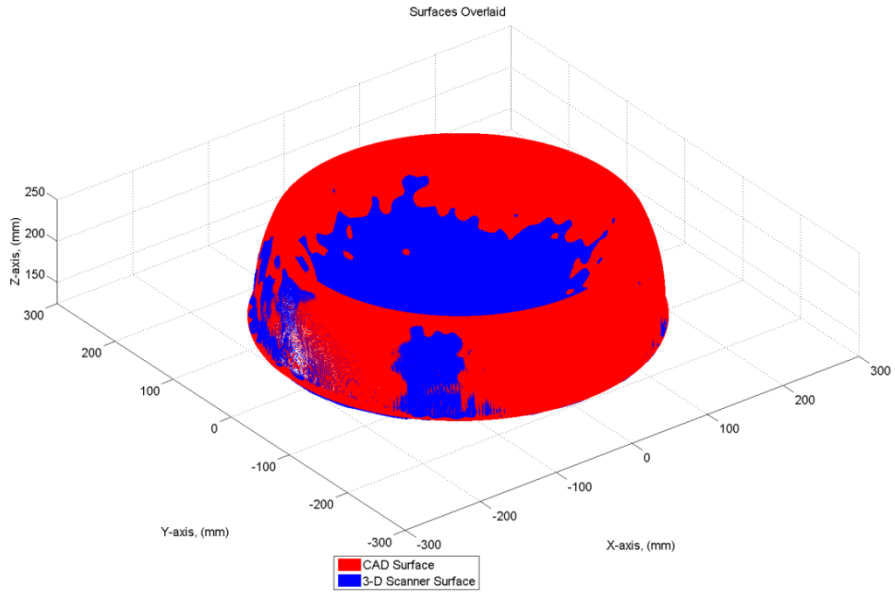

Figure 27 - Comparison of 3-D Printed Model and Scaned Model (Short)

The statistical regressions show an average accuracy of 3 mm, slightly worse than predicted by theory. High discrepancies over 50 mm were observed. To determine the source of these errors, a plot of the variation of Z_{diff} over the surface was produced, and is shown in Figure 28.

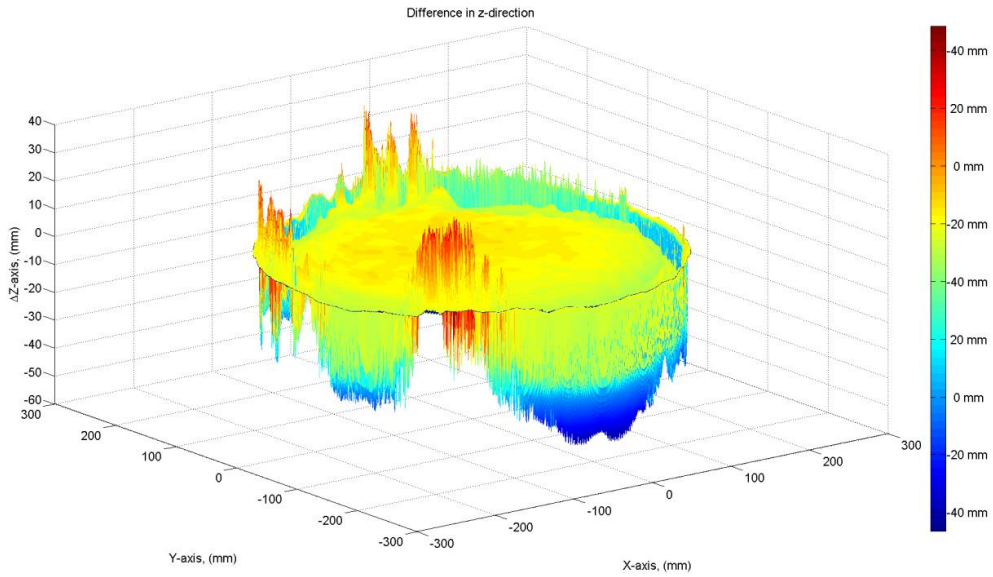

Figure 28 - Variation of Z_{diff} for Short Calibration Scan

The pattern of deviations suggests that the alignment between the models was not perfect during the comparison. This is unavoidable, and compensated for to the greatest extent possible using a coordinate transformation.

The entire process was repeated using a second model representing a much larger FF. The statistical results of the second calibration scan are given in Table 7 and the visual overlay is given in Figure 29.

Table 7 - Difference Between 3-D Printed Model and Scanned Model (Tall)

Avg. Z_{diff} (mm)	Standard Deviation (mm)	Avg. Euclidean Distance (mm)	Min. Euclidean Distance (mm)	Max. Euclidean Distance (mm)
-0.904	5.0289	3.0663	0.0000	50.0402

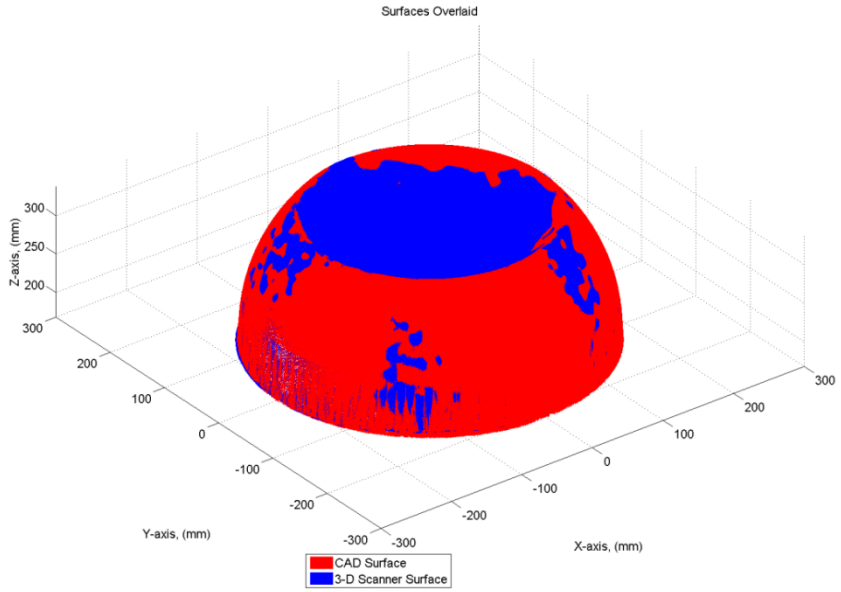

Figure 29 - Comparison of 3-D Printed Model and Scaned Model (Short)

The statistical analysis is nearly identical, showing the same average 3 mm offset with a maximum value of just over 50 mm. To confirm that this is largely due to model misalignment, Z_{diff} is again plotted over the surface, the results of which are depicted in Figure 30. Again, the alignment seems correct for the higher points, which are located closer to the scanners, but the lower points have greater discrepancies. The discrepancies are still directional, indicating model misalignment.

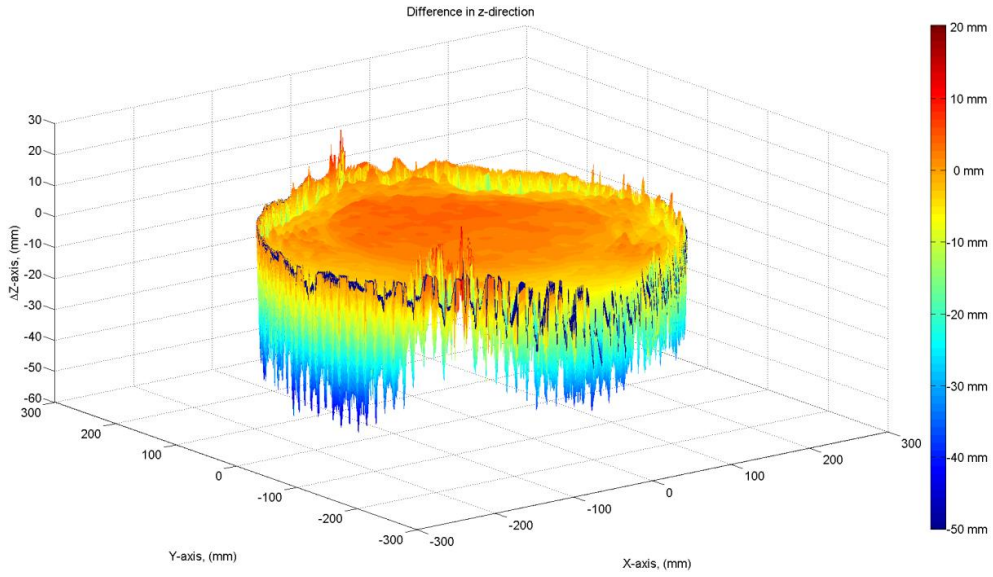

Figure 30 - Variation of Zdiff for Tall Calibration Scan

5.3.2 Comparison to Computational Model

The 3D scanning system can only record steady-state EDT geometries due to the extended duration required to capture all necessary points. Thus, the computational model is modified to display the results after the steady-state convergence is achieved and to skip the oscillations that normally follow. The results can then be compared to experimental data.

FF values beyond 50% exhibit well-behaved experimental shape, with a perfect dome and few, if any, wrinkles in the diaphragm. Folding does not occur at steady state for these high FF levels. Thus, only the steady state results for FFs up to and including 50% are presented in 10% increments. The results are shown in Figure 31 through Figure 35.

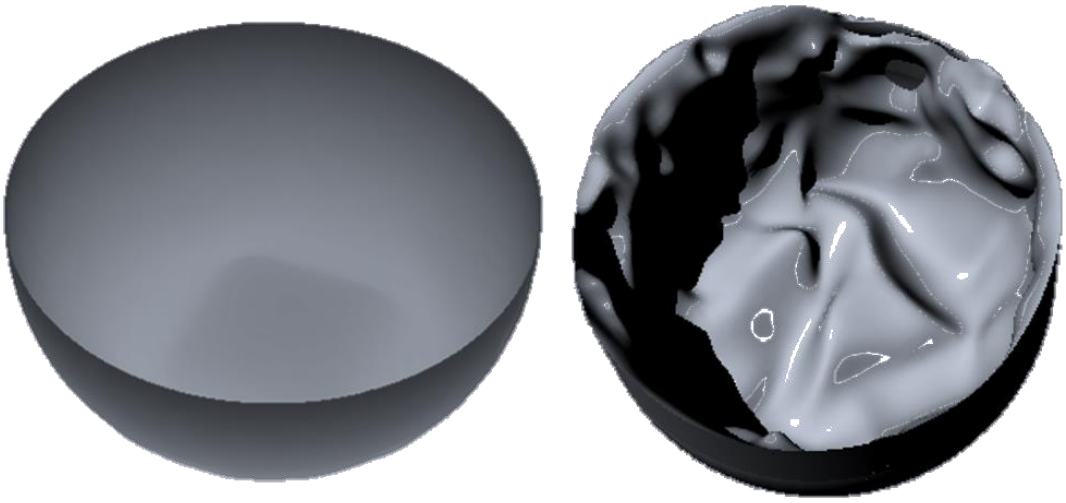

Figure 31 - Comparison of Computational and Experimental Rendering, FF=10%

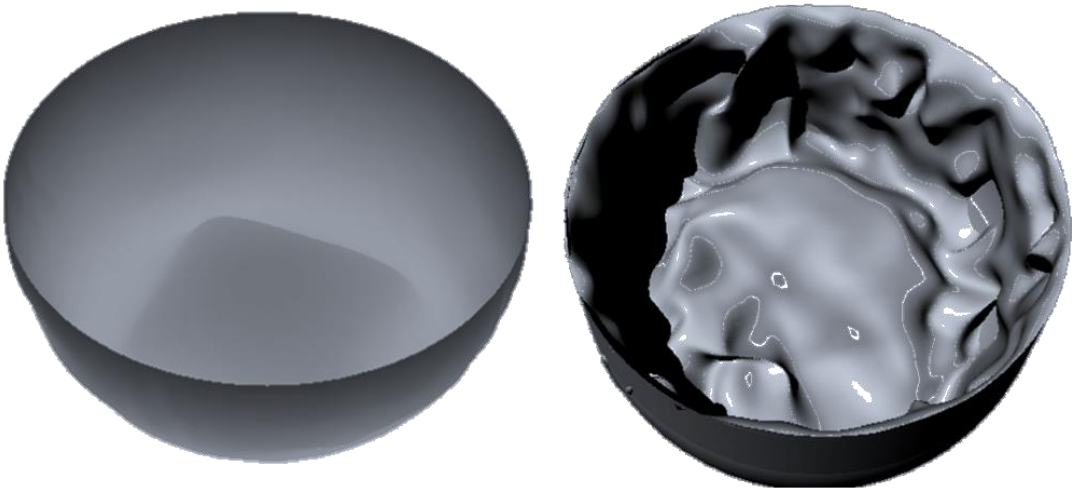

Figure 32 - Comparison of Computational and Experimental Rendering, FF=20%

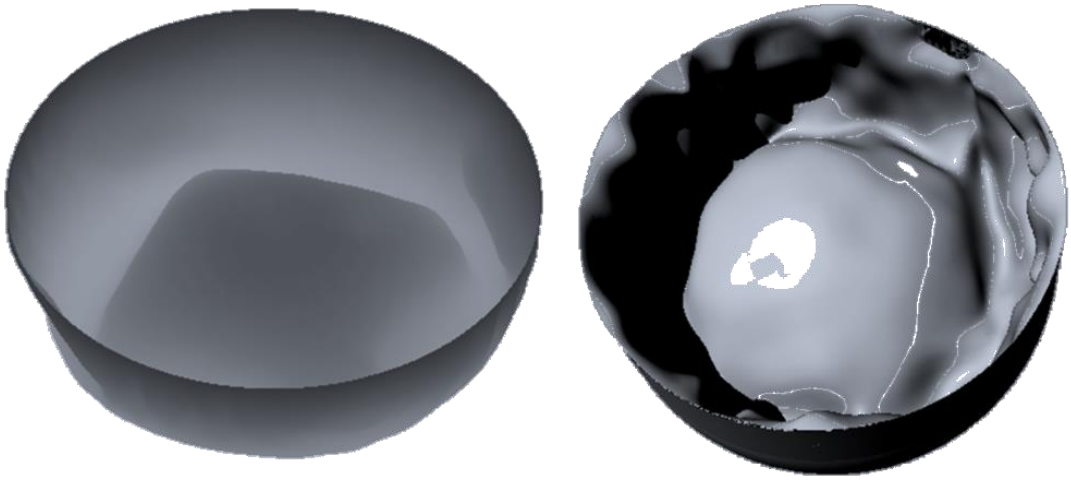

Figure 33 - Comparison of Computational and Experimental Rendering, FF=30%

Figure 34 - Comparison of Computational and Experimental Rendering, FF=40%

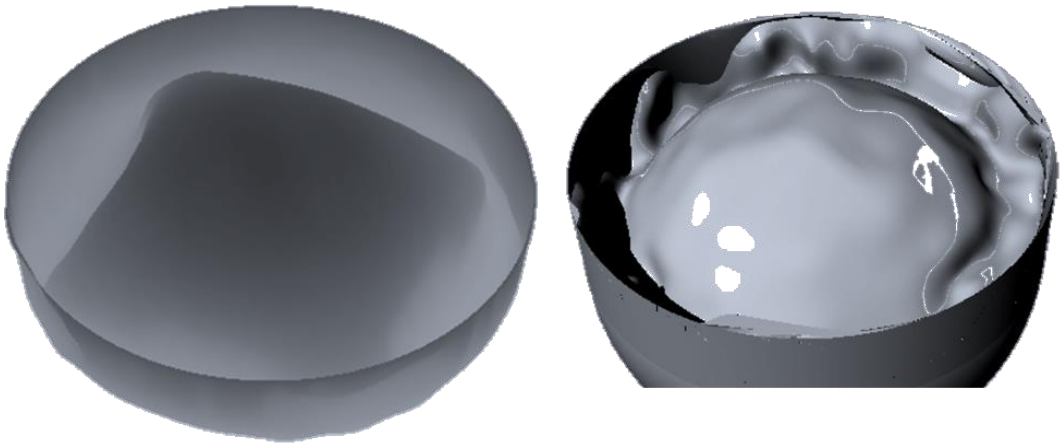

Figure 35 - Comparison of Computational and Experimental Rendering, FF=50%

As shown, the model exhibits a high degree of agreement in overall profile with experimental data. However, the folds and wrinkles are largely not present in the computational rendering. This is again an indication of an artificially high modulus of elasticity, resulting in an inflated flexural rigidity. Additionally, the folds appear somewhat random in the scanned images. This is an indication of some stochastic effects, perhaps resulting in small currents in the fluid phase or vibrations in the solid phase, which are not captured by the computational model. The lower the FF, the more pronounced these effects become. As the model is intended for analysis of tanks during ground transportation and launch pad winding, where the FF will be larger, this is not envisioned to cause a problem.

Also observed is the tendency for a cross-section of the model to exhibit a rounded-square geometry, rather than the natural circular geometry exhibited in the scans. This would naturally appear to be a meshing artifact which could be solved by increasing the spatial resolution, and consequently the temporal resolution to maintain stability. A parametric study in spatial resolution, however, reveals no change in the topology; the cross-sections remain rounded squares.

To examine the source of this discrepancy, a top-down view of the undeformed mesh is depicted in Figure 36. Concentric rings of the hemisphere are represented in the mesh as concentric squares of nodes. Thus, in an axisymmetric result, the circular cross section must also be represented by a square of nodes in computational space. This should not pose a problem, as the four sides of the square are free to bend, and could each form a quarter-circle, matching the desired experimental geometry. The problem is visibly depicted, however, at the corner nodes.

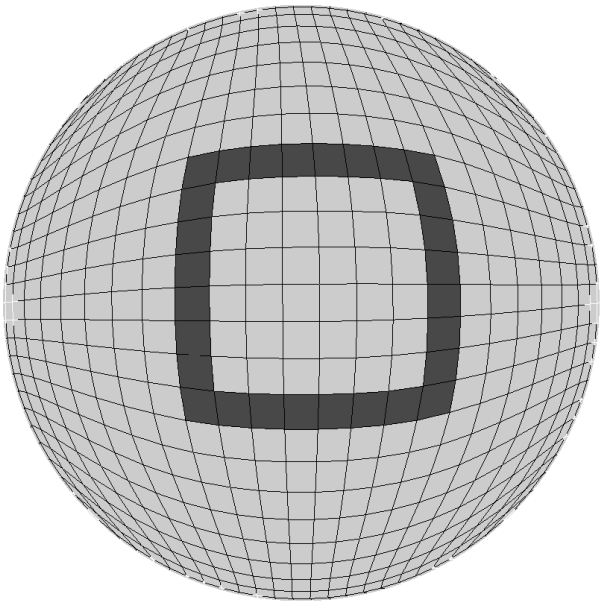

Figure 36 - Rounded-Square Cross-Section of Undeformed Mesh

As shown, the corners of the concentric squares are fairly unskewed, as a result of the forced mesh unskewing discussed in Chapter 3. For four quarter-circles along the edges to form a complete circle, they must meet at 180° angles, but the corner nodes force them to meet at 90° angles. The corner nodes cannot become skew to accommodate the circular cross section as a result of the shear-strain limiting nature of the algorithm used.

A number of attempts were made to combat this problem. Attempts to use a raw, skewed gnomonic projection, or even a partially skewed mesh where only the outermost rings were unskewed always resulted in edge lengths approaching zero in the highly skewed cells, leading to division by zero and ultimately model instability. Attempts were also made to eliminate the shear strain constraints, relying on the stretching constraints to automatically constrain the shear using the principle of Mohr's circle. Eliminating one shear constraint gave a preferential direction of shear, as would be expected, but eliminating both shear constraints resulted in a divergent algorithm due to the excessive degrees of freedom in the under-defined system. Attempts were also made to eliminate the shear strain constraints only along the corner nodes, represented by the diagonal elements of the mesh in computational space, but this also resulted in a divergent simulation for the same reason. With no attempts to solve the discrepancy resulting in a converged solution, additional work is needed and will be conducted by the ASAP Laboratory to solve the problem. It should be noted, however, that the transient simulation does provide a preferential direction aligned with one of the axes of the mesh, and therefore is only marginally affected by this discrepancy.

5.4 Chapter Summary

The ability to detect the depth of a point using an optical sensor allows for the complete three-dimensional reconstruction of an object as a digital model. Unlike conventional optical imaging, depth mapping allows the orientation and view settings to be set during post-processing and allows numerical data to be compared directly to experimentally gathered values in a quantitative way. The Xbox Kinect sensor, which utilizes a unique method for depth mapping, was proven to be an accurate means for experimental data gathering for steady state EDTs.

The Xbox Kinect sensor uses a star field mapping algorithm to uniquely identify points in its field of view and correlate them to an image projected from an offset source. The shift in position of a recognized element is a direct measure of the depth of that point. The method alleviated many of the problems faced by older methods for depth mapping. The primary downfalls are the high data rate required to support the device and the noise introduced by implementing multiple sensors. To solve the multiple sensor issues, only one sensor is activated at a time. Future iterations may use a staggered shutter to multiplex the sensors, or vibrating motors to blur the projections from each Kinect except to the corresponding sensing element. The high data rate was solved using a network of multiple computers with several USB Root Hub Controllers.

Comparing the computational results to the 3D scanned experimental data shows strong agreement. This is an indication that either method is a valid way to characterize the fluid distribution of spherical elastomeric diaphragm tanks at a steady state. Future developments would allow the scanning system to operate at real-time to capture transient data during a sinusoidal vibration.

Chapter 6
Conclusion

This thesis represents the culmination of research into a variety of methods for the characterization of fluid motion, including analytic, computational, and experimental methods, caused by sinusoidal vibration of elastomeric diaphragm tanks. A number of conclusions can be drawn from the results of these characterizations, and several lessons learned have identified areas where future studies could be conducted to create a more comprehensive understanding of elastomeric diaphragm tanks.

6.1 Summary of Contributions

The stated aim of this thesis is to characterize the fluid motion of spherical elastomeric diaphragm tanks undergoing sinusoidal oscillations. To this end, the specific contributions made herein are enumerated below.

1. Existing analytic models for the analysis of pressure-induced diaphragm deformations were evaluated, but their limitations were determined to be outside of the range of validity for the given application.
2. Existing computational methods used for rubber balloons were evaluated, but the assumptions of elastic membranes proved to introduce instabilities when applied to the given application.

3. A new analytic method was derived for the given application but required the assumption of a taut diaphragm. The dependence of slosh on the Bond and Weber Numbers was demonstrated.
4. A computational method for handling both the fluid and structure phases of the system with a proper set of assumptions for the given application was proposed and implemented.
5. The computational simulation was tested and validated against sinusoidal vibration test videos of EDTs, demonstrating consistency with experimental data.
6. A 3D scanning system was analyzed for its applicability to the analysis of steady-state EDTs and future application to transient studies.
7. Data collected using the 3D scanning system was compared to steady-state predictions of the computational model, increasing confiedence in the model.

6.2 Current and Future Work

The current computational work is valid only for the simplest case of a sinusoidal oscillation applied to a spherical tank with a flat diaphragm in order to apply assumptions to simplify the framework of the problem and focus only on the simulation method, rather than general applicability. Future work on this computational model will relax these restrictions for broader applicability. Accounting for non-spherical tanks requires a meshing algorithm that can adapt to geometries other than a hemisphere is necessary. Commercial meshing applications can be used, as long as the result can be expressed in a two-dimensional matrix of points with defined directions. The Cartesian coordinates of the points of the mesh can then be exported and read in, just as the external grid generator currently

implemented is used. Additionally, the shifting reference frame will necessitate the recalculation of the FluidHeight variable as a function of the FF for a non-spherical geometry. Depending on the specific geometry in question, this can be very algorithmically challenging.

ATK is currently investigating the use of ridges along the diaphragm to affect the adhesion of the liquid, which is not currently accounted for by the computational model. Additionally, this will stiffen the diaphragm in localized regions due to the added thickness. It is suspected that an equivalent constant-thickness diaphragm exists for a given ridge configuration, but additional research is needed to determine the equivalent thickness and effect of adhesion.

Future work is also needed in the experimental method proposed to improve spatial resolution and applicability to transient measurement. The use of higher-resolution depth scanners introduces the added complexity of even higher data transfer rates, necessitating the use of USB 3.0 and IEEE 1394 buses. Additionally, a higher response rate is desirable for transient studies. Data can be collected raw and in bulk, stored immediately to the disk, and post-processed at a later time. This will allow the entire apparatus to be affixed to an EDT during oscillation tests for transient quantitative validation of computational models. While future work will broaden the applicability, the existing work stands valid and useful in its own right for the analysis of EDT designs for potential material wear due to folding and rubbing.

Works Cited

[1] Kana, D.D., Dodge, F.T., "Study of Liquid Slosh in the Tracking and Data Relay Satellite Hydrazine Tanks," Southwest Research Institute, NASA CR-166745, September 1981.

[2] Ballinger, I.A., Sims, D., "Development of an EPDM Elastomeric Material for use in Hydrazine Propulsion Systems", AIAA 2003-4611, 2003.

[3] Ballinger, I.A., Lay, W.D., Tam, W.H., "Review and History of PSI Elastomeric Diaphragm Tanks", AIAA 95-2534, 1995.

[4] Tam, W.H., Ballinger, I.A., Jaekle, D.E., "Conceptual Design of Space Efficient Tanks," AIAA 2006-5058, 2006.

[5] Tam, W.H., Debreceni, M.J., Hesh, M.S., Nye, C.D., "Low Cost Derivative Tanks for Spacecraft and Launch Vehicles", AIAA 99-2831, 1999.

[6] Skouras, M., Thomaszewski, B., Bickel, B., Gross, M., "Computational Design of Rubber Balloons," *Eurographics*, Vol. 31, No. 2, 2012.

[7] Tam, W.H., Ballinger, I.A., Jaekle, D.E., "Tank Trade Studies – An Overview", AIAA 2008-4940, 2008.

[8] Coulbert, C.D., Cuddiny, E.F., Fedors, R.F., "Technical Memorandum 35-650: Long-Time Dynamic Compatibility of Elastomeric Materials with Hydrazine", NASA JPL, Pasadena, Ca, 1973.

[9] Tam, W.H., Taylor, J.R., "Design and Manufacture of a Propellant Tank Assembly," AIAA 97-2813, 1997.

[10] Fichter, W.B., "Some Solutions for the Large Deflections of Uniformly Loaded Circular Membranes," NASA Technical Paper 3658, Hampton, VA, July 1987.

[11] Timoshenko, S., Woinosky-Krieger, S., *Theory of Plates and Shells*, McGraw-Hill Classic Textbook Reissue, 1987.

[12] Young, W.C., Budynas, R.G., *Roark's Formulas for Stress and Strain*, 7th ed., McGraw-Hill, New York, 2002, Chap. 11.

[13] Levine, D.V., "Flexible Slosh Diaphragm Modeling and Simulation in Propellant Tanks," M.S. Thesis, Department of Mechanical and Aerospace Engineering, Florida Institute of Technology, Melbourne, Florida, 2014.

[14] Sances, D.J., Gangadharan, S.N., Sudermann, J.E., Marsell, B., "CFD Fuel Slosh Modeling of Fluid-Structure Interaction in Spacecraft Propellant Tanks with Diaphragms", AIAA 2010-2955, 2010.

[15] Berglund, M.D., Bassett, C.E., Kelso, J.M., Mishic, J., Schrage, D., "The Boeing Delta IV Launch Vehicle – Pulse-Settling Approach for Second-Stage Hydrogran Propellant Management," *Acta Astronautica*, Vol. 61, No. 1-6, June-August 2007, pp. 416-24.

[16] Vergalla, M., Zhou, R., Gutierrez, H.M., Kirk, D.R., "Experimental and Numerical Framework for Characterization of Slosh Dynamics," *International Review of Aerospace Engineering, ISSN 1973-7459*, Vol. 2, No. 1, July 2010.

[17] Zhou, R., Vergalla, M., Chiltalapati, S., Kirk, D.R., Gutierrez, H.M., "Experimental and Numerical Investigation of Liquid Slosh Behavior Using Ground-Based Platforms," *Journal of Spacecraft and Rockets*, Vol. 49, No. 6, 2012, pp.1194-1204; also AIAA Paper 2008-4667, Jul. 2008.

[18] Chintalapati, S., Kirk, D.R., "Parametric Study of Propellant Tank Slosh Baffle", AIAA 2008- 4750, 2008.

[19] Vergalla, M., Livesay, G., Kirk, D.R., Gutierrez, H.M., "Experimental and Numerical Investigation of Reduced Gravity Fluid Slosh Dynamics," AIAA 2008-4667, 2008.

[20] Faure, J.M.,, Vergalla, M., Zhou, R., Chintalapati, S., Gutierrez, H.M., Kirk, D.R., "Experimental Platform for the Study of Liquid Slosh Dynamics Using Sounding Rockets," *International Review of Aerospace Engineering*, Vol. 3, No. 1, pp.59-67.

[21] Chintalapati, S., Holicker, C.A., Schulman, R.E., Contreras, E., Gutierrez, H.M., Kirk, D.R., "Design of Experimental Platform for Acquisition of Liquid Slosh Data aboard the International Space Station", AIAA 2012-4297, 2012.

[22] Chintalapati, S., Holicker, C.A., Schulman, R.E., Wise, B.D., Lapilli, G.D., Gutierrez, H.M., Kirk, D.R., "Update on SPHERES Slosh for Acquisition of Liquid Slosh Data aboard the ISS", AIAA2013-3903, 2013.

[23] Chintalapati, S., "Design of Experimental Platform for Acquisition of Liquid Slosh Data aboard the International Space Station," M.S. Thesis, Department of Mechanical and Aerospace Engineering, , Florida Institute of Technology, Melbourne, Florida, 2012.

[24] Coleman, M.P., *An Introduction to Partial Differential Equations with MATLAB*, 1st ed., Chapman and Hall, London, 2004.

[25] Connolly, M.L., "Computation of Molecular Volume," *Journal of the American Chemical Society*, Vol. 107, No. 5, 1985, pp. 1118-24.

[26] White, F.M., *Fluid Mechanics*, 7th ed., McGraw-Hill, New York, 2010.

[27] Goldenthal, R., Harmon, D., Fattal, R., Bercovier, M., Grinspun, E., "Efficient Simulation of Inextensible Cloth,", ACM Transaction on Graphics, Proceedings of SIGGRAPH2007, 2007.

[28] Hoffman, K.A., Chang, S.T., *Computational Fluid Dynamics*, Vol. 1, 4th ed. EES Books, Wichita, 2000.

[29] Chen, C.G., Xiao, F., Li, X.K., Yang, Y., "A multi-moment transport model on cubed-sphere grid," *International Journal for Numerical Methods in Fluids*, No. 67, 2011, pp. 1993-2014.

[30] Beer, F.P., Johnston, E.R., DeWolf, J.T., Mazurek, D.F., *Mechanics of Materials*, 6th ed., McGraw-Hill, New York, 2011.

[31] Bender, J., Weberb, D., Diziol, R., "Fast and Stable Cloth Simulation Based on Multi-Resolution Shape Modeling", Computers & Graphics 37(8), 2013, pp. 945-952.

[32] Bender, J., Bayer, D., Diziol, R., "Dynamic Simulation of Inextensible Cloth," *IADIS International Journal on Computer Science in Information Systems*, Vol. 4, No. 2, 2009, pp. 86-102.

[33] Thomaszewski, E., Fabst, S., Strasser, W., "Continuum-Based Strain Limiting," Computer Graphics Forum 2009 28(2), pp. 569-76

[34] Wang, H., O'Brien, J., Ramamoorthi, R., "Multi-Resolution Isotropic Strain Limiting," ACM Trans Graph 2010 29(6), pp. 156:1-156:10.

[35] Jakel, I.R., "Analysis of Hyperelastic Materials with MECHANICA: Theory and Application Examples," Presentation for the 2nd AXSIM, Technische Universität, Chemnitz, 2010.

[36] Ballester, J., Pheatt, C., "Using the Xbox Kinect sensor for positional data acquisition," *American Journal of Physics*, Vol. 81, No. 71, 2013, pp. 71-77.

[37] Andrew, M., Henry, F., "Reducing Interference Between Multiple Structured Light Depth Sensors Using Motion," Proceedings of IEEE Virtual Reality Conference, 2012.

[38] Butler, A., Izadi, S., Hilliges, O., Molyneaux, D., Hodges, S., Kim, D., "Shake'n'Sense: Reducing interference for overlapping structured light depth cameras," Conference on Human Factors in Computing Systems, 2012.

[39] Ramamurthy, G., Ashenayi, K., "Comparative Study of the FireWire™ IEEE 1394 Protocol with the Universal Serial Bus and Ethernet," , Midwest Symposium on Circuits and Systems, 2002.

Appendix A
Main Driver Program

```
function mov =
GetSteadyState(dt,GridSize,ErrorLimit,Radius,Thickness,rhoMembrane,
E,rho,FillFraction,Frequency,Amplitude)
%% Constants and Initial Conditions
gravity=-9.81;
FluidHeight=-Radius*median(roots([-0.25 0 0.75 0.5-FillFraction]));
BendDamping=10;
kappa=E*(1/12)*(Thickness^3);
Frequency=Frequency*2*pi;
t=0; converged=0; frame=0; accel=0;
mov(1:(1/dt)+1) = struct('cdata',[],'colormap',[]);
[X,Y,Z] = GridGenerator(GridSize,Radius);
vX=(X-X);vY=vX;vZ=vX;
%% Compute Mass Matrix and Apply Boundary Conditions
[NodeArea] = FindNodeArea(X,Y,Z,GridSize);
M=rhoMembrane*Thickness*NodeArea;
Minv=1./M;
M(1,:)=0; M(:,1)=0; M(GridSize,:)=0; M(:,GridSize)=0;
Minv(1,:)=0; Minv(:,1)=0; Minv(GridSize,:)=0; Minv(:,GridSize)=0;
%% Get Resting Diaphragm Topology
[LengthX, MFBX, MFFX] = GridLengthMap(X,Y,Z,GridSize,Minv,0,1);
[LengthY, MFBY, MFFY] = GridLengthMap(X,Y,Z,GridSize,Minv,1,0);
[LengthPS, MFBPS, MFFPS] = GridLengthMap(X,Y,Z,GridSize,Minv,1,1);
[LengthNS, MFBNS, MFFNS] = GridLengthMap(X,Y,Z,GridSize,Minv,-1,1);
[LengthXB, MFBXB, MFFXB] = GridLengthMap(X,Y,Z,GridSize,Minv,0,2);
[LengthYB, MFBYB, MFFYB] = GridLengthMap(X,Y,Z,GridSize,Minv,2,0);
ErrorLimit=ErrorLimit*sum(sum(abs(LengthX)+abs(LengthY)+abs(LengthP
S)+abs(LengthNS)));
%% Begin Simulation
while(converged<2)
    clc;
    t=t+
    %% Compute pressure
    if converged==1
        accel=-(Frequency^2)*Amplitude*sin(Frequency*t);
    end
    Pressure=rho*(accel*X+gravity*Z-
FluidHeight*sqrt(accel^2+gravity^2));
    [NX,NY,NZ] = surfnorm(X,Y,Z);
    [NodeArea] = FindNodeArea(X,Y,Z,GridSize);
    %% Compute unconstrained response
     [FbX,FbY,FbZ,kfd] =
InternalForces(X,Y,Z,LengthXB,kappa,NX,NY,NZ,2,0)+InternalForces(X,
Y,Z,LengthYB,kappa,NX,NY,NZ,0,2);
    c=2*(M.*kfd).^0.5;
```

```
    FX=FbX+NodeArea.*Pressure.*NX-c.*vX;
    FY=FbY+NodeArea.*Pressure.*NY-c.*vY;
    FZ=FbZ+NodeArea.*Pressure.*NZ+M*gravity-c.*vZ;
    %% Kinematic effect of unconstrained forces
    aX=FX.*Minv; aY=FY.*Minv; aZ=FZ.*Minv;
    vX=vX+aX*dt; vY=vY+aY*dt; vZ=vZ+aZ*dt;
    X=X+vX*dt; Y=Y+vY*dt; Z=Z+vZ*dt;
    %% Satisfy Material Spring Relaxation Constraints and
Collisions
    [X,Y,Z] = ContainerCollisionCheck(X,Y,Z,GridSize,Radius);
    error=100;
    while error>ErrorLimit
        [X Y Z error1] =
ConstrainToPoint(X,Y,Z,MFBX,MFFX,LengthX,0,1);
        [X Y Z error2] =
ConstrainToPoint(X,Y,Z,MFBY,MFFY,LengthY,1,0);
        [X Y Z error4] =
ConstrainToPoint(X,Y,Z,MFBNS,MFFNS,LengthNS,-1,1);
        [X Y Z error3] =
ConstrainToPoint(X,Y,Z,MFBPS,MFFPS,LengthPS,1,1);
        error=error1+error2+error3+error4;
    end
    for BendDamp = 1:BendDamping
        [X Y Z error] =
ConstrainToPoint(X,Y,Z,MFBXB,MFFXB,LengthXB,0,2);
        [X Y Z error] =
ConstrainToPoint(X,Y,Z,MFBYB,MFFYB,LengthYB,2,0);
    end
    error=100;
    while error>ErrorLimit
        [X Y Z error1] =
ConstrainToPoint(X,Y,Z,MFBX,MFFX,LengthX,0,1);
        [X Y Z error2] =
ConstrainToPoint(X,Y,Z,MFBY,MFFY,LengthY,1,0);
        [X Y Z error4] =
ConstrainToPoint(X,Y,Z,MFBNS,MFFNS,LengthNS,-1,1);
        [X Y Z error3] =
ConstrainToPoint(X,Y,Z,MFBPS,MFFPS,LengthPS,1,1);
        error=error1+error2+error3+error4;
    end
    [X,Y,Z] = ContainerCollisionCheck(X,Y,Z,GridSize,Radius);
    if converged==0 && t>=1
        converged=1;
        t=0;
    end
    if t>10
        frame=frame+1;
        XP=X+Amplitude*sin(Frequency*t);
        XI=interp2(XP,2,'spline');
        YI=interp2(Y,2,'spline');
        ZI=interp2(Z,2,'spline');
```

```
            surf(XI,YI,ZI,'FaceColor','interp','EdgeColor','none');
            axis equal;
            axis off;
            grid off;
            view(-65, 45);
            colormap(cool);
            xlim([-Radius-Amplitude Radius+Amplitude]);
            pause(0.01);
            mov(frame)=getframe(gcf);
            if t>=11
                converged=2;
            end
        end
    end
    end
```

Appendix B
Grid Generator

```
function [X,Y,Z] = GridGenerator(GridSize,Radius)
%-------------------------------------------------------------------
%GridGenerator.
% [X,Y,Z] = GridGenerator(GridSize,Radius) returns the position
% components of the 3-D surface (X,Y,Z), for a hemisphere using a
% modified gnomonic projection method when given a cubic grid
% resolution (GridSize), and a sphere radius (Radius).
%
% Created by: Darren V. Levine 4-8-14
%-------------------------------------------------------------------
x=1;y=2;z=3;
iii=0;
sphereLimit=pi/2.01;
for x0=-sphereLimit:2*sphereLimit/(GridSize-1):sphereLimit;
    for y0=-sphereLimit:2*sphereLimit/(GridSize-1):sphereLimit;
        iii=iii+1;
        aa=Radius*sqrt(3)/3;
        xa=aa*tan(x0);
        ya=aa*tan(y0);
        ra=sqrt(aa^2+xa^2+ya^2);
        yyn(iii)=Radius*xa/ra;
        zzn(iii)=-Radius*(-aa)/ra;
        xxn(iii)=Radius*ya/ra;
    end
end
P=[xxn;yyn;zzn]; % x=P(x,:),y=P(y,:),z=P(z,:)
for i=1:GridSize
    X(i,:)=P(x,1+(i-1)*GridSize:GridSize*i);
    Y(i,:)=P(y,1+(i-1)*GridSize:GridSize*i);
    Z(i,:)=P(z,1+(i-1)*GridSize:GridSize*i);
end
%% Spiral Mapping:
i=round(GridSize/2);
j=i+1;
k=0;
b=0;
k=k+1;
xS(k)=X(i,j); yS(k)=Y(i,j); zS(k)=Z(i,j);SM(k,:)=[i;j];
j=j-1;
k=k+1;
xS(k)=X(i,j); yS(k)=Y(i,j); zS(k)=Z(i,j);SM(k,:)=[i;j];
while k<GridSize^2-GridSize*2
    b=b+1;
    for n=1:b
        i=i+1;
```

```
        j=j;
        k=k+1;xS(k)=X(i,j); yS(k)=Y(i,j);
zS(k)=Z(i,j);SM(k,:)=[i;j];
    end
    b=b+1;
    for n=1:b
        i=i;
        j=j+1;
        k=k+1;xS(k)=X(i,j); yS(k)=Y(i,j);
zS(k)=Z(i,j);SM(k,:)=[i;j];
    end
    b=b-1;
    for n=1:b+1
        i=i-1;
        j=j;
        k=k+1;xS(k)=X(i,j); yS(k)=Y(i,j);
zS(k)=Z(i,j);SM(k,:)=[i;j];
    end
    b=b+1;
    for n=1:b+1
        i=i;
        j=j-1;
        k=k+1;xS(k)=X(i,j); yS(k)=Y(i,j);
zS(k)=Z(i,j);SM(k,:)=[i;j];
    end
end
b=b+1;
for n=1:b
    i=i+1;
    j=j;
    k=k+1;xS(k)=X(i,j); yS(k)=Y(i,j); zS(k)=Z(i,j);SM(k,:)=[i;j];
end
b=b;
for n=1:b
    i=i;
    j=j+1;
    k=k+1;xS(k)=X(i,j); yS(k)=Y(i,j); zS(k)=Z(i,j);SM(k,:)=[i;j];
end
%% Circular Segment Creation
a=-1;
b=0;
c=1;
for arccount=1:GridSize/2
    a=a+2;
    b=b+2;
    d=a*2+b*2+c-1;
    Arcs(arccount,:)=[c;d];
c=d+1;
end
%% Track angle in 90 degree increments
for i=1:GridSize
```

```
    for j=1:GridSize
        if Y(i,j)>0 && X(i,j)>0
            beta(i,j)=atand(Y(i,j)/X(i,j));
            elseif Y(i,j)<0 && X(i,j)>0
            beta(i,j)=360-atand(-Y(i,j)/X(i,j));
        elseif Y(i,j)<0 && X(i,j)<0
            beta(i,j)=180+atand(Y(i,j)/X(i,j));
        elseif Y(i,j)>0 && X(i,j)<0
            beta(i,j)=180-atand(Y(i,j)/-X(i,j));
        else
            fprintf('error')
        break
        end
    end
end
%% Determine Correct Rotational Position
for k=1:GridSize/2-1
    c=Arcs(k,1);
    d=Arcs(k,2);
    kki=SM(c:d,1);
    kkj=SM(c:d,2);
    clear anglearc1
    arcnumber=length(SM(c:d,1));
    for ii=1:arcnumber
        anglearc1(ii)=beta(kki(ii),kkj(ii));
    end
    requiredAngle=[360:-360/arcnumber:360/arcnumber];
    for iii=1:arcnumber-1
        if anglearc1(iii)<anglearc1(iii+1)
            g=iii;
        end
    end
    RequiredAngleOrdered = [requiredAngle(end-g+1:end)...
    requiredAngle(1:end-g)];
    ThetaChange=(RequiredAngleOrdered-anglearc1).*...
    ((Radius-zS(c:d))./Radius);
    % Rotating points to corrected position
    xxm=X;
    yym=Y;
    for ii=1:arcnumber
        xxn(c+ii-1)=xxm(kki(ii),kkj(ii)).*cosd(ThetaChange(ii))...
        -yym(kki(ii),kkj(ii)).*sind(ThetaChange(ii));
        yyn(c+ii-1)=xxm(kki(ii),kkj(ii)).*sind(ThetaChange(ii))...
        +yym(kki(ii),kkj(ii)).*cosd(ThetaChange(ii));
    end
end
%operations to the last spiral arm with corrections for the end
edge:
k=GridSize/2;
c=Arcs(k,1);
d=length(SM(:,1));
```

```
kki=SM(c:d,1);
kkj=SM(c:d,2);
clear anglearc1 requiredAngle RequiredAngleOrdered ThetaChange
arcnumber=length(SM(c:d,1));
for ii=1:arcnumber
    anglearc1(ii)=beta(kki(ii),kkj(ii));
end
requiredAngle=[360-45:-270/arcnumber:270/arcnumber+45];
RequiredAngleOrdered=requiredAngle;
ThetaChange=(RequiredAngleOrdered-anglearc1);
% Rotating points to corrected position
xxm=X;
yym=Y;
for ii=1:arcnumber
    xxn(c+ii-1)=xxm(kki(ii),kkj(ii)).*cosd(ThetaChange(ii))...
    -yym(kki(ii),kkj(ii)).*sind(ThetaChange(ii));
    yyn(c+ii-1)=xxm(kki(ii),kkj(ii)).*sind(ThetaChange(ii))...
    +yym(kki(ii),kkj(ii)).*cosd(ThetaChange(ii));
end
%Convert temporary values into global X Y coordinate system
for k=1:length(SM(:,1))
    ki=SM(k,1);
    kj=SM(k,2);
    X(ki,kj)=xxn(k);
    Y(ki,kj)=yyn(k);
end
Z=-Z;
end
```

Appendix C
Rest Conditions

```
function [Length,MFB,MFF] =
GridLengthMap(X,Y,Z,GridSize,Minv,ioff,joff)
    X2 = circshift(X,[-ioff -joff]);
    Y2 = circshift(Y,[-ioff -joff]);
    Z2 = circshift(Z,[-ioff -joff]);
    Minv2 = circshift(Minv,[-ioff -joff]);
    XD=X2-X; YD=Y2-Y; ZD=Z2-Z;
    Length=sqrt(XD.^2 + YD.^2 + ZD.^2);
    MFB = Minv./(Minv+Minv2);
    MFF = Minv2./(Minv+Minv2);
    MFB(isnan(MFB))=0;
    MFF(isnan(MFF))=0;
    if ioff<0
        MFF(1:-ioff,:)=0;
        MFB(1:-ioff,:)=0;
    else
        if ioff>0
            MFF(GridSize+1-ioff:GridSize,:)=0;
            MFB(GridSize+1-ioff:GridSize,:)=0;
        end
    end
    if joff<0
        MFF(:,1:joff)=0;
        MFB(:,1:joff)=0;
    else
        if joff>0
            MFF(:,GridSize+1-joff:GridSize)=0;
            MFB(:,GridSize+1-joff:GridSize)=0;
        end
    end
end
```

Appendix D
Mesh Cell Area

```
function [NodeArea] = FindNodeArea(X,Y,Z,GridSize)
%% Finding the area at each face patch:
PatchArea(1:GridSize+1,1:GridSize+1)=0; %preallocation
parfor i = 1:GridSize-1
    for j = 1:GridSize-1
        vec1=[X(i,j) Y(i,j) Z(i,j)];
        vec2=[X(i,j+1) Y(i,j+1) Z(i,j+1)];
        vec3=[X(i+1,j) Y(i+1,j) Z(i+1,j)];
        vec4=[X(i+1,j+1) Y(i+1,j+1) Z(i+1,j+1)];
        aa=vec2-vec1;bb=vec3-vec1;cc=vec4-vec1;
        PatchArea(i,j)=0.5*(norm(cross(aa,cc))+norm(cross(bb,cc)));
    end
end
%% Averaging the face areas to create a node area:
NodeArea(1:GridSize,1:GridSize)=0; %preallocation
for i = 1:GridSize-1
    for j = 1:GridSize-1

NodeArea(i+1,j+1)=(PatchArea(i,j)+PatchArea(i+1,j)+PatchArea(i,j+1)
+PatchArea(i+1,j+1))/4;
    end
end
end
```

Appendix E
Unconstrained Response

```
function [Fbx,Fby,Fbz,keq] =
InternalForces(X,Y,Z,Rest,kappa,NX,NY,NZ,ioff,joff)
    X2 = circshift(X,[-ioff -joff]);
    Y2 = circshift(Y,[-ioff -joff]);
    Z2 = circshift(Z,[-ioff -joff]);
    XM = circshift(X,[-ioff/2 -joff/2]);
    YM = circshift(Y,[-ioff/2 -joff/2]);
    ZM = circshift(Z,[-ioff/2 -joff/2]);
    NXM = circshift(NX,[-ioff/2 -joff/2]);
    NYM = circshift(NY,[-ioff/2 -joff/2]);
    NZM = circshift(NZ,[-ioff/2 -joff/2]);
    XC = (X+X2)/2; YC = (Y+Y2)/2; ZC = (Z+Z2)/2;
    XD=X2-X; YD=Y2-Y; ZD=Z2-Z;
    deltalength = sqrt(XD.^2 + YD.^2 + ZD.^2);
    d = abs(real(sqrt((Rest./2).^2 - (deltalength./2).^2)));
    Keq = 48*kappa./Rest.^2;
    signX = sign(abs(sqrt((XM-(XC+NXM)).^2+(YM-(YC+NYM)).^2+(ZM-
(ZC+NZM)).^2))-...
        abs(sqrt((XM-(XC-NXM)).^2+(YM-(YC-NYM)).^2+(ZM-(ZC-
NZM)).^2)));
    Fb = signX.*d*Keq;
    Fbx = Fb.*NXM; Fby = Fb.*NYM; Fbz = Fb.*NZM;
    Fbx = circshift(Fbx,[ioff/2 joff/2]);
    Fby = circshift(Fby,[ioff/2 joff/2]);
    Fbz = circshift(Fbz,[ioff/2 joff/2]);

end
```

Appendix F
Constrain To Point

```
function [X, Y, Z, errors] =
ConstrainToPoint(X,Y,Z,MFB,MFF,Rest,ioff,joff)
    X2 = circshift(X,[-ioff -joff]);
    Y2 = circshift(Y,[-ioff -joff]);
    Z2 = circshift(Z,[-ioff -joff]);
    XD=X2-X; YD=Y2-Y; ZD=Z2-Z;
    deltalength = sqrt(XD.^2 + YD.^2 + ZD.^2);
    error = deltalength-Rest;
    errors=sum(sum(abs(error)));
    multA=error.*MFB./deltalength;
    multS=error.*MFF./deltalength;
    xA=XD.*multA;
    yA=YD.*multA;
    zA=ZD.*multA;
    xS=XD.*multS;
    yS=YD.*multS;
    zS=ZD.*multS;
    xS = circshift(xS,[ioff joff]);
    yS = circshift(yS,[ioff joff]);
    zS = circshift(zS,[ioff joff]);
    X = X + xA-xS;
    Y = Y + yA-yS;
    Z = Z + zA-zS;
end
```

Appendix G
Container Collision Check

```
function [X,Y,Z] = ContainerCollisionCheck(X,Y,Z,GridSize,Radius)
parfor i=2:GridSize-1
    for j=2:GridSize-1
        vectormag=norm([X(i,j) Y(i,j) Z(i,j)]);
        if abs(vectormag)>Radius*1.001
            vectordist=[X(i,j) Y(i,j) Z(i,j)];
            DirectionV=vectordist/vectormag;
            X(i,j)=Radius*DirectionV(1);
            Y(i,j)=Radius*DirectionV(2);
            Z(i,j)=Radius*DirectionV(3);
        end
    end
end
end
```